Cell Reports

Article

Endothelial Tpl2 regulates vascular barrier function via JNK-mediated degradation of claudin-5 promoting neuroinflammation or tumor metastasis

Graphical abstract

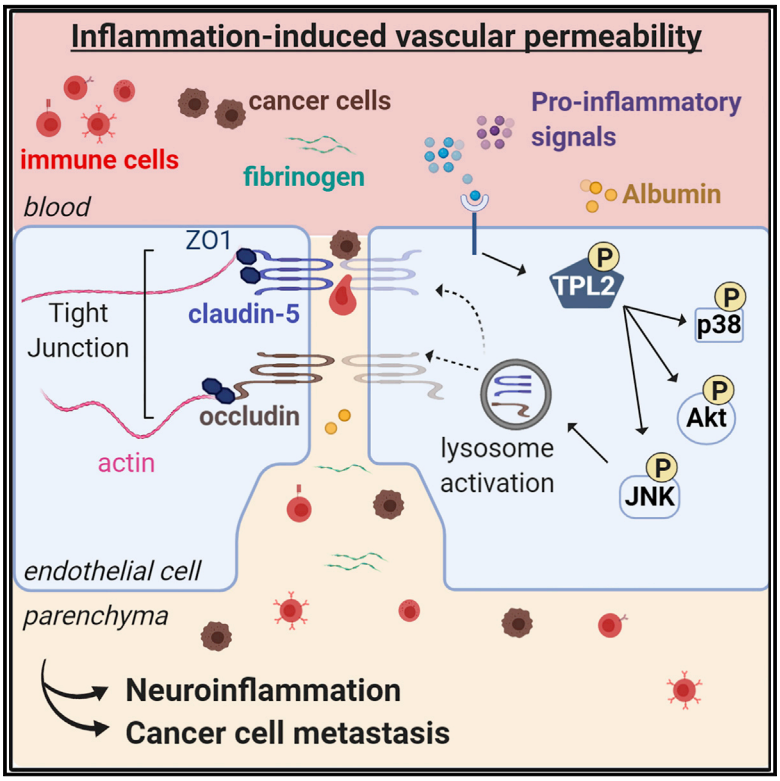

Highlights

- Endothelial-specific function of Tpl2 linked to vascular barrier permeability
- Endothelial cell (EC)-specific Tpl2 ablation reduces neuroinflammation in EAE
- Endothelial Tpl2 ablation reduces tumor nodule formation in lung metastasis model
- Mechanistically, EC Tpl2 induces JNK-mediated lysosomal degradation of claudin-5

Authors

Aikaterini Nanou, Mara Bourbouli, Stefania Vetrano, Ute Schaeper, Steven Ley, George Kollias

Correspondence

geokollias@med.uoa.gr

In brief

Increased vascular permeability and leakage facilitate metastatic and immune cell infiltration in inflammation. Nanou et al. show that endothelial-specific Tpl2 regulates vascular barrier permeability through JNK-mediated lysosomal degradation of tight junction protein claudin-5. Genetic or pharmacologic Tpl2 ablation in mice reduces neuroinflammation and cancer cell metastasis, highlighting its therapeutic potential.

Nanou et al., 2021, Cell Reports *35*, 109168
May 25, 2021
https://doi.org/10.1016/j.celrep.2021.109168

CellPress

Cell Reports

CellPress
OPEN ACCESS

Article

Endothelial Tpl2 regulates vascular barrier function via JNK-mediated degradation of claudin-5 promoting neuroinflammation or tumor metastasis

Aikaterini Nanou,[1] Mara Bourbouli,[1] Stefania Vetrano,[2,3] Ute Schaeper,[4] Steven Ley,[5,6] and George Kollias[1,7,8,*]
[1]Institute for Bioinnovation, Biomedical Science Research Center (BSRC) "Alexander Fleming," Vari, Attika, Greece
[2]Department of Biomedical Sciences, Humanitas University, Rozzano, Italy
[3]IBD Center, Humanitas Research Hospital, Rozzano, Italy
[4]Silence Therapeutics GmbH, Berlin, Germany
[5]Immune Cell Signalling Laboratory, The Francis Crick Institute, London, UK
[6]Imperial College, London, UK
[7]Department of Physiology, Medical School, National and Kapodistrian University of Athens, Athens, Greece
[8]Lead contact
*Correspondence: geokollias@med.uoa.gr
https://doi.org/10.1016/j.celrep.2021.109168

SUMMARY

Increased vascular permeability and leakage are hallmarks of several pathologies and determine disease progression and severity by facilitating inflammatory/metastatic cell infiltration. Using tissue-specific genetic ablation in endothelial cells, we have investigated *in vivo* the role of Tumor progression locus 2 (Tpl2), a mitogen-activated protein kinase kinase kinase (MAP3K) member with pleiotropic effects in inflammation and cancer. In response to proinflammatory stimuli, endothelial Tpl2 deletion alters tight junction claudin-5 protein expression through inhibition of JNK signaling and lysosomal degradation activation, resulting in reduced vascular permeability and immune cell infiltration. This results in significantly attenuated disease scores in experimental autoimmune encephalomyelitis and fewer tumor nodules in a hematogenic lung cancer metastasis model. Accordingly, pharmacologic inhibition of Tpl2 or small interfering RNA (siRNA)-mediated Tpl2 knockdown recapitulates our findings and reduces lung metastatic tumor invasions. These results establish an endothelial-specific role for Tpl2 and highlight the therapeutic potential of blocking the endothelial-specific Tpl2 pathway in chronic inflammatory and metastatic diseases.

INTRODUCTION

Tpl2 kinase (Tumor progression locus 2, also known as mitogen-activated protein kinase 8 [MAP3K8] or Cot), originally identified as a proto-oncogene, encodes a serine/threonine kinase that belongs to the MAP3K family (Vougioukalaki et al., 2011). Tpl2 is involved in both innate and adaptive immune responses: it becomes activated by an array of proinflammatory factors (e.g., interleukin-1 [IL-1], lipopolysaccharide [LPS], and tumor necrosis factor [TNF]) and, in a stimulus- and cell-specific manner, it activates MAPKs, p38α, JNK, and extracellular signal-regulated kinase (ERK) through MKK1/2, MKK3/6, and nuclear factor κB (NF-κB) (Xu et al., 2018). It is critical for the production of inflammatory mediators, such as IL-1, Cox2, PGE2, TNF, and IL-6 (Das et al., 2005; Dumitru et al., 2000; Eliopoulos et al., 2002; McNab et al., 2013; Pattison et al., 2016), and it regulates IL-10, IL-12, type I interferon (IFN), and hepatocyte growth factor (HGF) production in different models of inflammation (Kaiser et al., 2009; Koliaraki et al., 2012; Papoutsopoulou et al., 2006; Tomczak et al., 2006). Although Tpl2 mutations in human cancers are considered rare events (Clark et al., 2004; Newman et al., 2019), it has been reported to be overexpressed or constitutively active in various cancer types and inflammatory disorders (Vougioukalaki et al., 2011). It has been widely suggested that Tpl2 is an attractive target to promote anti-cancer and anti-inflammatory strategies for specific cancer types and inflammatory conditions, due to its broad regulation of immune responses (Gantke et al., 2012; Lee et al., 2015).

Experimental autoimmune encephalomyelitis (EAE), the most commonly used model of multiple sclerosis (MS), induces the priming of myelin-specific T cells in secondary lymphoid organs through MOG (myelin oligodendrocyte glycoprotein) immunization and pertussis toxin administration, which eventually results in immune cell infiltration in the central nervous system (CNS). Interestingly, we previously showed that Tpl2 deletion can attenuate the phenotype of EAE through irradiation-resistant non-hematopoietic cell types without affecting Th17 cell priming and differentiation (Sriskantharajah et al., 2014). It has also been suggested that Tpl2 deficiency in *ex vivo* astrocytes impairs activation of the IL-17R-TAK1 axis, thereby affecting the IL-17-stimulated expression of chemokines and proinflammatory cytokines that, in turn, affects the development of EAE (Xiao et al.,

2014). The effect of Tpl2 deletion in stromal cells, and not immune cells, is of particular importance, as it shifts the paradigm of its anti-inflammatory impact. Here, we focused on endothelial cells (ECs), which control the passage of blood-borne molecules and allow extravasation of white blood cells into and out of the bloodstream (Hawkins and Davis, 2005; Obermeier et al., 2013). The endothelial barrier consists of tight junctions (TJs) and adherent junctions (AJs), which are formed by specialized transmembrane and cytoplasmic proteins, such as occludin, claudin-3, claudin-5, junctional adhesion molecules, and zonula occludens (ZO-1) for TJ, and vascular endothelial (VE)-cadherin and catenins for AJ (Rubin and Staddon, 1999; Stamatovic et al., 2008). These structures respond to tissue-specific requirements and physiological stimuli by changing their expression, functional properties, and permeability to promote ionic and solute fluxes, as well as passage of cells (Obermeier et al., 2013; Rubin and Staddon, 1999). Inflammatory (IFN-γ, TNF-α, and IL-1β) and angiogenic (VEGF) stimuli lead to increased vascular permeability and vascular leakage, which is linked to the pathogenesis of an array of diseases due to the loss of EC junctional integrity, including obstruction of respiratory airways during pulmonary disorders (Groeneveld, 2002), circulatory collapse in sepsis (Shiels et al., 1998), cancer metastasis (Mierke et al., 2008), and stroke and MS (Obermeier et al., 2013). Several signal transduction pathways have been implicated in barrier permeability, such as cellular PTKs, RhoGTPases, MAPKs, NF-κB, and PI-3K pathways (Lassmann et al., 1994; Stamatovic et al., 2008).

In this study, we determined the endothelial role of Tpl2 in the regulation of vascular permeability using tissue-specific deletion of Tpl2 in mice. Tpl2 deficiency of ECs affected MAPKs activation under inflammatory stimuli, attenuated the downregulation of TJ protein levels, and restricted the inflammation-induced vascular permeability *in vitro* and *in vivo*. Our results establish an endothelial-specific function for Tpl2 in controlling barrier-associated proteins and vascular permeability through inhibition of JNK signaling and lysosomal degradation, which significantly affects the development of inflammation, EAE, and cancer cell metastasis. These findings highlight the therapeutic potential of Tpl2 inhibition as a means to regulate vascular permeability in both acute and chronic inflammatory conditions.

RESULTS

Endothelial Tpl2 regulates clinical EAE severity, CNS inflammation, and demyelination

We have previously shown that Tpl2 regulates the onset and severity of EAE based on experiments with Tpl2$^{-/-}$ mice, and specifically, that Tpl2 expression in radiation-resistant cells was sufficient to promote EAE (Sriskantharajah et al., 2014). To explore the contribution of Tpl2 expression in different cell populations to the disease phenotype, the most relevant radiation-resistant cells were studied. After the generation of mice lacking Tpl2 expression in all cells (Tpl2^{DD}), tissue-specific Tpl2 ablation was performed in astrocytes (Tpl2^{AstrKO}), microglia (Tpl2^{MicrKO}), neurons (Tpl2^{NeurKO}), and ECs (Tpl2^{ECKO}). Consistent with previous reports, Tpl2^{DD} mice exhibited significantly attenuated disease scores in comparison with control mice (Tpl2^{FF}) after EAE induction (Figure 1A), whereas Tpl2^{AstrKO} (GFAP-Cre), Tpl2^{MicrKO} (both CD11b-Cre and tamoxifen-induced CX3CR1-CreERT2), and Tpl2^{NeurKO} (Nestin-Cre) mice did not show significantly altered disease scores in comparison with controls (Figures S1A–S1D). Notably, significantly reduced scores were seen in Tpl2^{ECKO} (Tie1-Cre) mice, indicating a role for endothelial-specific Tpl2 in the development of disease (Figure 1A). Histological evaluation of spinal cords stained for myelin and inflammatory infiltration showed reduced levels of demyelination and CNS inflammation in Tpl2^{ECKO} mice compared with controls, while immunohistochemical staining for astrocytes (glial fibrillary acidic protein [GFAP]) and macrophages/microglia (F4/80) indicated attenuated patterns of astrocytic staining and macrophage/microglia infiltration/activation (Figures 1B and S1E).

Since the Tie1-Cre mouse, used here for endothelial targeting, also produces off-target deletions in the hematopoietic compartment (Gustafsson et al., 2001), the tissue specificity of this mouse line was further characterized through the use of the ROSAmTmG (TmG) reporter mice, where membrane-bound GFP (mGFP) protein expression is activated upon Cre-induced recombination. Endothelial-specific Tpl2 deletion was confirmed with western blot analysis, and as previously reported (Gustafsson et al., 2001), 70% deletion in the endothelial compartment was seen, with 10%–30% deletion in the hematopoietic cells (Figure S2). To identify whether this off-target deletion significantly affects the hematopoietic compartment of Tpl2^{ECKO} mice, the numbers and functional properties of T and B cells from lymphoid tissues of naive Tpl2^{ECKO} and Tpl2^{FF} mice were examined with no detectable differences (Figures S3 and S4).

To further study the differences in the disease phenotype observed between Tpl2^{FF}, Tpl2^{DD}, and Tpl2^{ECKO} mice, flow cytometric analysis was performed to assess the inflammatory cells present in inguinal lymph nodes or infiltrating the spinal cord during disease progression. At the pre-symptomatic stage of EAE (9 days post immunization [dpi]), no differences in resident or infiltrating inflammatory cells were seen between Tpl2^{FF}, Tpl2^{DD}, and Tpl2^{ECKO} mice, nor a shift in the production of inflammatory cytokines, such as IL-17, IFN-γ, and IL-10 (Figure S5). At the peak of the disease (16 dpi) and in accordance with the clinical phenotype, the absolute numbers of all four major inflammatory cell types infiltrating the spinal cord (CD4$^+$ T helper, CD8$^+$ T cytotoxic, CD11b$^+$ macrophages, and B220$^+$ B cells) were significantly reduced in Tpl2^{DD} and Tpl2^{ECKO} mice compared with control Tpl2^{FF} mice (Figures 1C and S5G). Furthermore, the absolute numbers of the CD4$^+$ cells expressing IL-17, IFN-γ, and IL-10 were significantly decreased in both Tpl2^{DD} and Tpl2^{ECKO} compared with Tpl2^{FF} mice, while the average per-cell expression levels of cytokines were not significantly different between the three genotypes (Figure 1D). Since the increased infiltration of inflammatory cells suggested increased blood-brain barrier (BBB) disruption, immunohistochemistry was performed in EAE spinal cords for albumin and fibrinogen, markers associated with the opening of BBB (Argaw et al., 2009). Tpl2^{FF} mice exhibited increased BBB disruption compared with both Tpl2^{ECKO} and Tpl2^{DD} mice, suggesting that Tpl2 absence confers a protective effect against the BBB breakdown seen in EAE. Specifically, Tpl2^{FF} mice at the pre-symptomatic phase of EAE showed increased albumin and fibrinogen deposition in the spinal cord compared with Tpl2^{DD} and Tpl2^{ECKO} mice, without any changes

CellPress
OPEN ACCESS

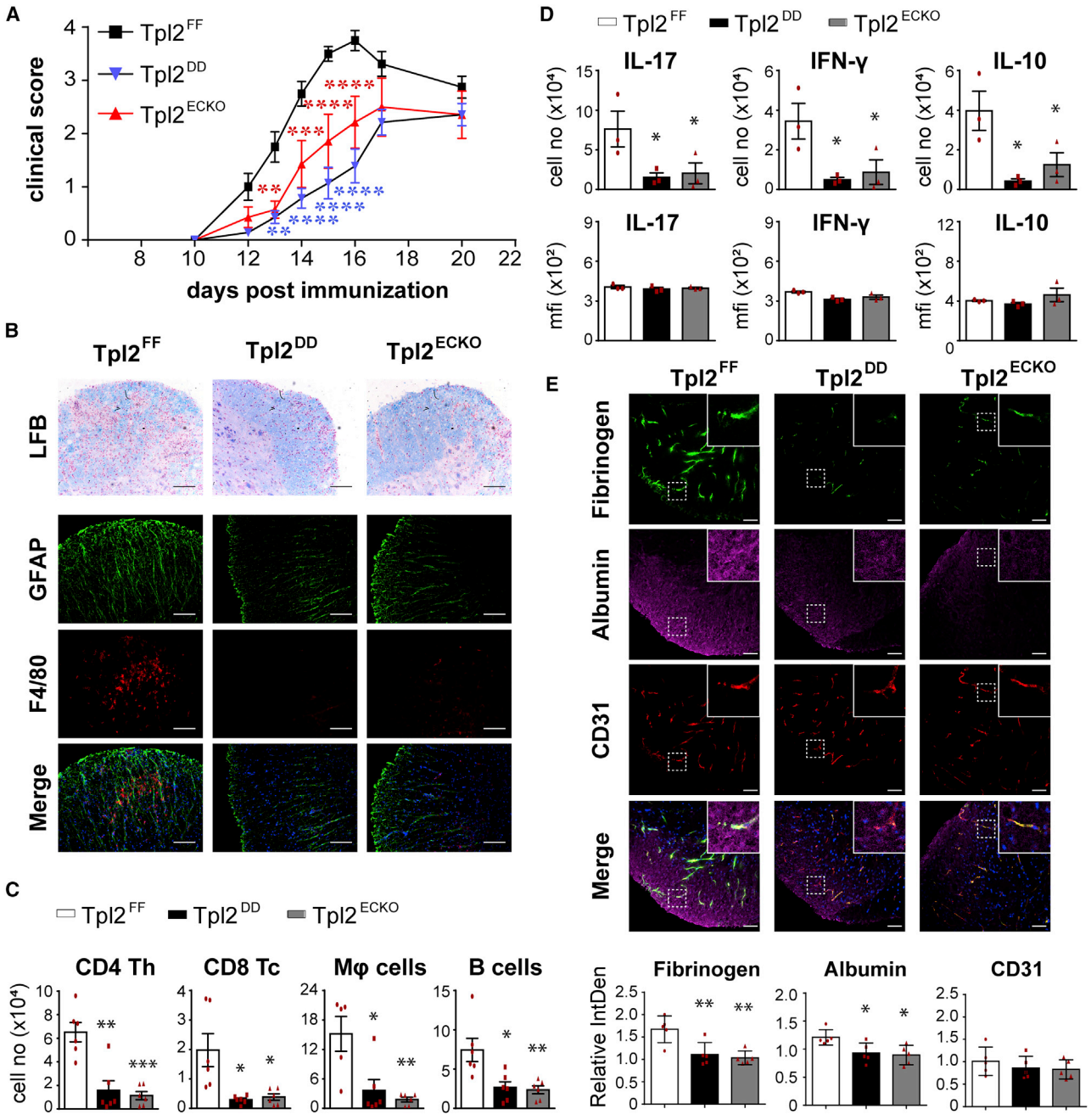

Figure 1. Endothelial Tpl2 regulates disease severity, demyelination, and inflammatory infiltration in the EAE model

(A) Disease progression in MOG-immunized Tpl2^{FF}, Tpl2^{DD}, and Tpl2^{ECKO} (n = 7–8 mice/genotype, two-way ANOVA, Bonferroni's multiple comparisons test, ±SEM).

(B) Spinal cord histology sections from Tpl2^{FF}, Tpl2^{DD}, and Tpl2^{ECKO} mice at 16 dpi (days post immunization). Sections were stained with Luxol fast blue (LFB) to assess demyelination, or with antibodies against GFAP for astrocytes, and F4/80 for macrophages/microglia (scale bar, 60 μm).

(C and D) Flow cytometric analysis of leukocyte- and cytokine-producing cells from the spinal cord of Tpl2^{FF}, Tpl2^{DD}, and Tpl2^{ECKO} mice at 16 dpi. Absolute cell number quantification or mean fluorescent intensity (MFI) is shown (n = 3–6 mice/genotype, unpaired two-tailed Student's t test, ±SEM).

(E) Spinal cord sections from EAE Tpl2^{FF}, Tpl2^{DD}, and Tpl2^{ECKO} mice (9 dpi) co-stained against albumin, fibrinogen, and CD31 (scale bar, 50 μm). Insets of dashed areas are shown at the top right corner of each image.

Quantification was performed using relative integrated density values, normalized per experiment (n = 5 mice per genotype/condition, one-way ANOVA, Tukey's multiple comparisons test, ±SEM). Data are representative of three (A–C and E) or two experiments (D).

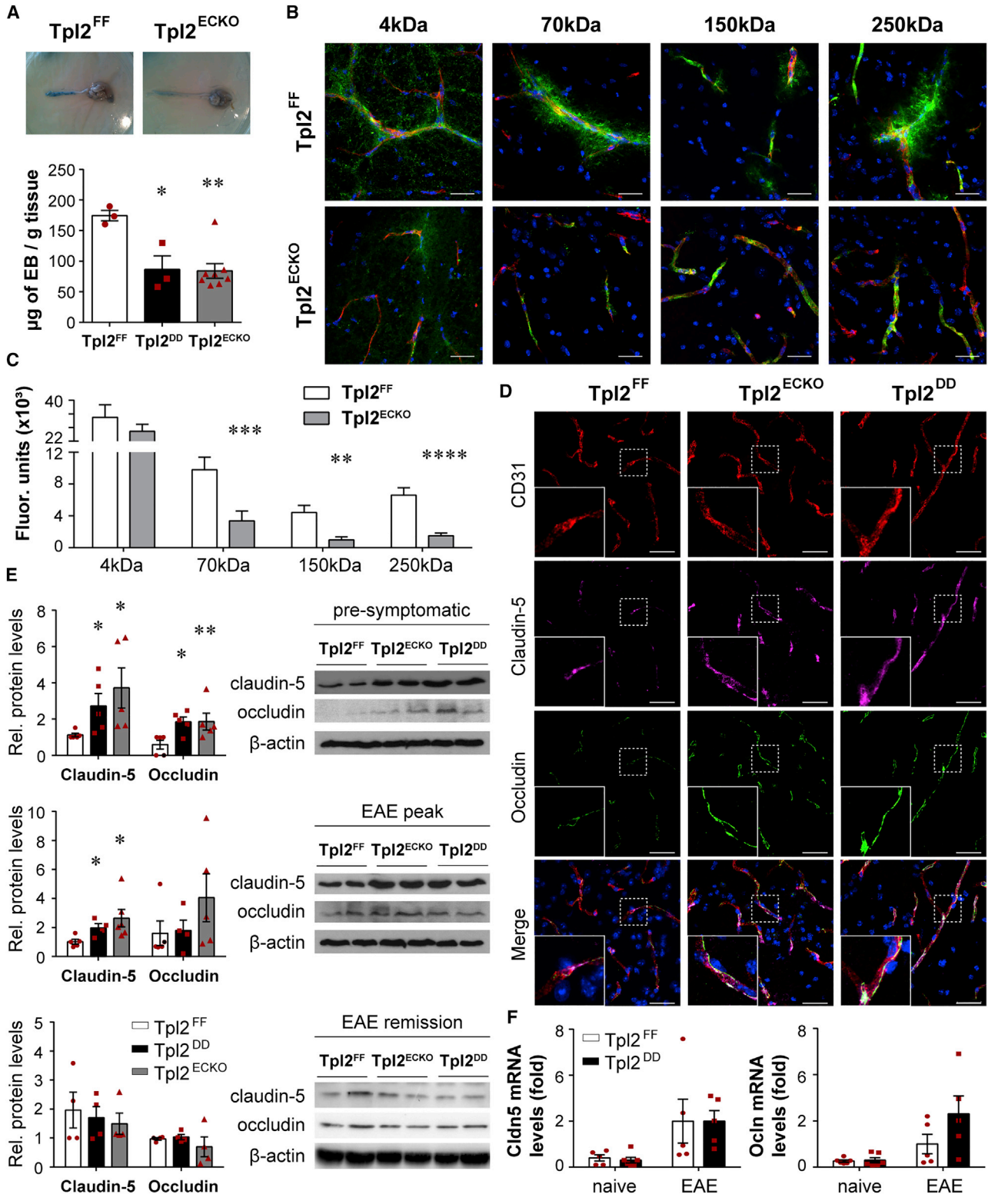

Figure 2. Tpl2 modulates EC functional molecules associated with barrier properties *in vivo* in the EAE model

(A) At 10 dpi of EAE, Tpl2^{FF}, Tpl2^{DD}, and Tpl2^{ECKO} mice were intravenously (i.v.) injected with Evan's blue (EB), and 24 h later, quantification of the extravasated EB was performed by formamide extraction from spinal cord. Top panel shows representative spinal cord/brain images from Tpl2^{FF} and Tpl2^{ECKO} mice, and bottom panel shows EB spectrophotometric quantification corrected for tissue weight (n = 3–8 mice per genotype, unpaired two-tailed Student's t test, ±SEM).

(legend continued on next page)

in vasculature architecture or coverage (Figure 1E). No differences were seen between the genotypes under basal conditions, suggesting that the changes are induced upon inflammatory stimuli (Figures S1F and S1G). Further characterization was performed using flow cytometric analysis for the expression of CD31 and VEGFR2, molecules involved in AJs, angiogenesis, permeability, and general endothelial properties, showing that they were unaffected by Tpl2 deficiency following EAE (Figure S6). Expression of ICAM-1 and VCAM-1, EC molecules essential for spinal cord infiltration and upregulated during inflammation (Rothhammer et al., 2011), were also unaffected by Tpl2 deficiency either in total or EC-specific Tpl2 ablation (Figure S6).

Taken together, these data establish an endothelial-specific role for Tpl2 in promoting the infiltration of myelin-primed autoimmune and inflammatory cells into the CNS, leading to the development of encephalomyelitis.

Endothelial Tpl2 regulates the physiology of BBB during EAE

To address the impact of endothelial-specific Tpl2 ablation on the physiology of the BBB, spinal cord permeability was studied through intravenous injections of Evan's blue (EB) or fluorescein isothiocyanate (FITC)-dextran of different molecular weights (MWs) in $Tpl2^{ECKO}$ and $Tpl2^{FF}$ mice at 10 days after EAE induction. Spectrophotometric measurement of extravasated EB showed significantly higher levels of EB infiltrating the CNS in $Tpl2^{FF}$ spinal cords compared with $Tpl2^{ECKO}$ (Figure 2A). Fluorescent imaging of the 4 kDa FITC-dextran molecule showed a similar degree of diffusion in both genotypes; however, higher diffusion of the 70, 150, and the 250 kDa MW FITC-dextran molecules were seen in the spinal cord of $Tpl2^{FF}$ compared with $Tpl2^{ECKO}$ mice (Figures 2B and 2C).

We then identified two key molecules involved in endothelial TJ formation, claudin-5 and occludin, which exhibited altered patterns of expression during the EAE disease progression. Both proteins showed increased expression in immunofluorescence experiments of spinal cords at the pre-symptomatic phase of EAE of $Tpl2^{ECKO}$ and $Tpl2^{DD}$ mice compared with control mice (Figure 2D), whereas much lower expression is seen in naive mice without any differences between the genotype (Figure S7). Additionally, significantly increased levels of claudin-5 expression were observed in $Tpl2^{DD}$ and $Tpl2^{ECKO}$ mice compared with $Tpl2^{FF}$ mice both at 9 and 16 dpi, as analyzed through western blot analysis, whereas during EAE remission (25 dpi) no significant differences were seen, recapitulating the clinical phenotype previously seen (Figure 2E). A similar pattern of expression was seen in occludin at the early stages of EAE; however, its expression was reduced with disease progression approximating the pattern of $Tpl2^{FF}$ mice. During EAE remission, no differences were seen in both claudin-5 and occludin protein levels among all genotypes. By contrast, when ECs were extracted from the spinal cord of mice at the pre-symptomatic phase of EAE, no significant differences in claudin-5 or occludin mRNA levels were seen between $Tpl2^{FF}$ and $Tpl2^{ECKO}$ mice (Figure 2F), suggesting that Tpl2 regulation of claudin-5 and occludin occurs post-transcriptionally.

Thus, in the absence of endothelial Tpl2 and despite sensitization by pertussis toxin and MOG-induced anti-myelin autoimmunity, the BBB remains relatively intact preventing inflammatory and autoimmune infiltration, and clinical EAE.

Endothelial Tpl2 reduces lung metastatic nodules in the B16Bl6 melanoma model

We next investigated whether the endothelial Tpl2 regulation of vascular permeability could also prove important in tumor cell metastasis. Thus, the effect of endothelial-specific Tpl2 deletion was evaluated in the lung metastasis model of B16Bl6 melanoma cells through examination of metastatic nodules 12 days after intravenous administration of the cancer cells. Significantly reduced formation of metastatic nodules was observed in $Tpl2^{ECKO}$ compared with $Tpl2^{FF}$ mice, as well as reduced number of inflammatory cells (T cells, B cells, and macrophages) in and proximal to tumors in $Tpl2^{ECKO}$ mice, probably due to the reduction in the overall number of tumors (Figures 3A and 3B). To assess the potential impact in the vascular architecture, especially in vascularization/angiogenesis within the tumors, ECs of lung sections were stained for CD31 and NG2, a pericyte marker. Microscopic examination of the tumors and lungs in $Tpl2^{FF}$ and $Tpl2^{ECKO}$ revealed no major differences in tumor vascularization, and the general architecture of the lung vessels appeared intact with similar pericyte coverage (Figure 3C). In addition, immunohistochemistry was performed against the endothelial permeability markers and TJ proteins claudin-5 and ZO-1, both of which exhibited increased expression in the absence of endothelial Tpl2, as assessed by fluorescent imaging and measurement of integrated fluorescent density of the proteins (Figure 3D). Similar results were also obtained at 19 days post tumor cell injection (data not shown), suggesting a persistent effect in the absence of Tpl2. Finally, no differences were seen between the

(B and C) At 9–10 dpi of EAE, $Tpl2^{FF}$ and $Tpl2^{ECKO}$mice were i.v. injected with FITC-dextran of 4, 70, 150, and 250 kDa, which were left to circulate. Spinal cord samples were collected and stained with CD31 (red) and DAPI (blue) to visualize vessels and nuclei, respectively (n = 4–6 mice/group; scale bar, 30 μm). Quantification of permeability using the Imaris software (unpaired two-tailed Student's t test, ±SEM).

(D) Spinal cord histology sections from EAE $Tpl2^{FF}$, $Tpl2^{DD}$, and $Tpl2^{ECKO}$ mice (9 dpi) co-stained against claudin-5, occludin, and CD31 (n = 3–5 mice per genotype/condition; scale bar, 30 μm). Insets of dashed areas are shown at the bottom left corner of each image.

(E) Western blot analysis in protein lysates from spinal cords of $Tpl2^{FF}$, $Tpl2^{DD}$, and $Tpl2^{ECKO}$ mice at 9 (pre-symptomatic), 16 (EAE peak), and 25 dpi (EAE remission) against claudin-5, occludin, and β-actin (n = 4–5 mice per genotype). Representative western blots depict two different mice per genotype and condition. Quantification was performed relative to β-actin, and $Tpl2^{DD}$ and $Tpl2^{ECKO}$ mice were compared with $Tpl2^{FF}$ mice (unpaired two-tailed Student's t test, ±SEM).

(F) RT-PCR performed in ECs isolated from the spinal cord of either naive or 9 dpi EAE $Tpl2^{FF}$ and $Tpl2^{DD}$ mice (n = 5 mice per genotype/condition, unpaired two-tailed Student's t test, ±SEM).

Data are representative of three (A–D) or average values of three experiments (E and F).

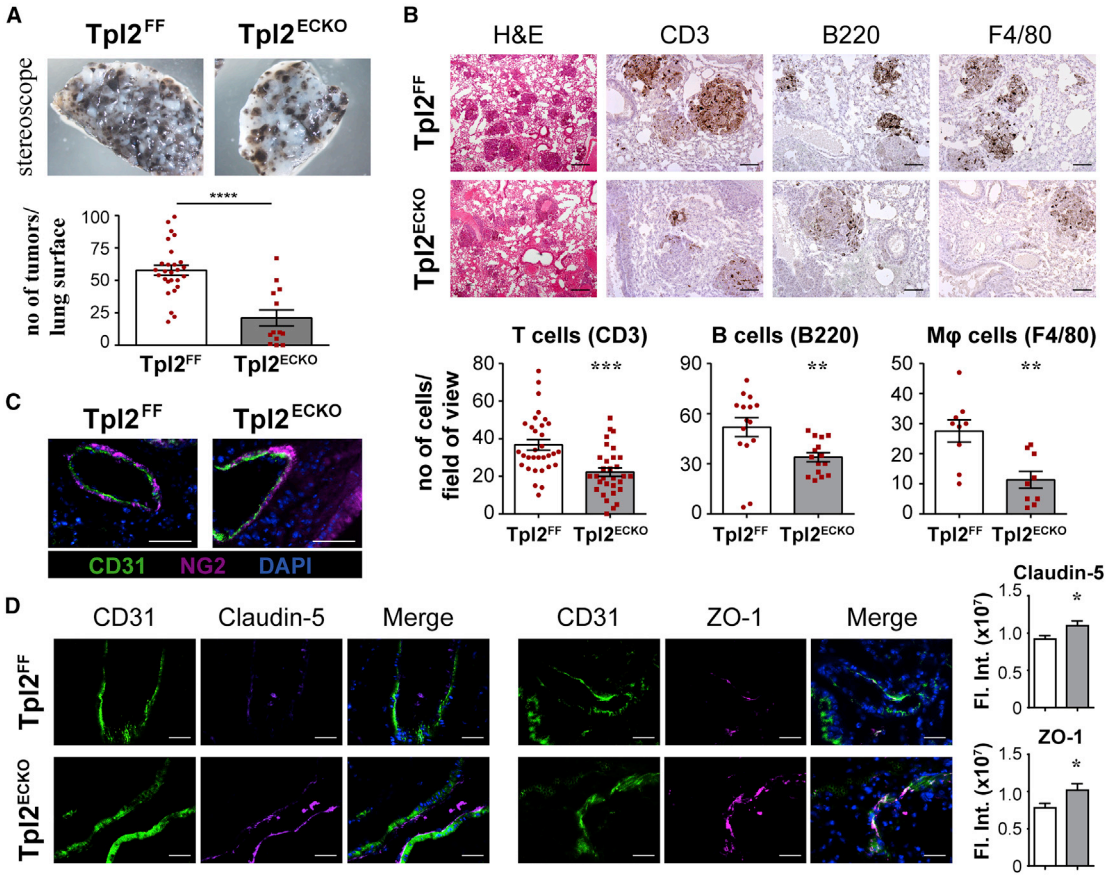

Figure 3. Tpl2 absence reduces lung metastatic nodules in the B16Bl6 melanoma model

(A and B) B16Bl6 melanoma cells were i.v. transferred to Tpl2^{FF} and Tpl2^{ECKO} mice, which were sacrificed at 12 dpi.

(A) Stereoscopic images of lungs are shown from Tpl2^{FF} and Tpl2^{ECKO}, and quantification of tumors per lung surface was performed by counting (>20 fields of view/genotype, unpaired two-tailed Student's t test, ±SEM).

(B) Lung sections were stained for H&E and with antibodies against CD3, B220, and F4/80 (scale bars: 150 μm for H&E and 60 μm for CD3, B220, and F4/80). Quantification of cell numbers for T cells, B cells, and macrophages was performed per field of view (>20 fields of view/genotype, unpaired two-tailed Student's t test, ±SEM).

(C) Lung sections were co-stained for NG2, CD31, and DAPI. Scale bar, 25 μm.

(D) Lung sections were co-stained for either CD31 and claudin-5 or CD31 and ZO-1. Nuclei were visualized with DAPI staining (scale bar, 25 μm). Quantification of integrated density of protein fluorescent intensity was performed for claudin-5 and ZO-1 (>20 fields of view/genotype, n = 4–8 mice/genotype, unpaired two-tailed Student's t test, ±SEM).

Data are representative of two experiments (A–D).

genotypes in naive mice of either vessel architecture or TJ protein expression (Figures S7B–S7D).

Taken together with the data from the EAE model, these results establish a key role of endothelial Tpl2 in controlling tumor cell metastasis by regulating TJ proteins and vascular permeability.

Endothelial Tpl2 enhances vascular permeability through JNK and lysosomal degradation regulation

To validate the role of Tpl2 in the regulation of vascular barriers under physiological conditions, *in vivo* permeability assays were performed. Tpl2^{FF} and Tpl2^{ECKO} mice received intravenously EB dye and 2 h later an intradermal injection of IL-1β in the lateral skin using the adjacent side as control through saline administration (Figure 4A). Whereas enhanced permeability was induced by IL-1β in both Tpl2^{FF} and Tpl2^{ECKO} mice compared with saline-treated tissue, significant attenuation was observed in the IL-1β-induced permeability in the Tpl2^{ECKO} mice compared with Tpl2^{FF} mice. To further characterize the reduced permeability seen in the absence of endothelial Tpl2, different FITC-dextran molecules were tested after intradermal IL-1β treatment in the right ear of Tpl2^{FF} and Tpl2^{ECKO} mice (Figure 4B). In particular, the 4 kDa FITC-dextran diffused completely in both genotypes after IL-1β administration, whereas the 70 kDa FITC-dextran showed higher diffusion in Tpl2^{FF} than in Tpl2^{ECKO} mice. In the latter, FITC-dextran remained to a greater extent in the vessels and co-localized with the endothelial marker von Willebrand factor (vWf), similar to the saline-treated ears, whereas

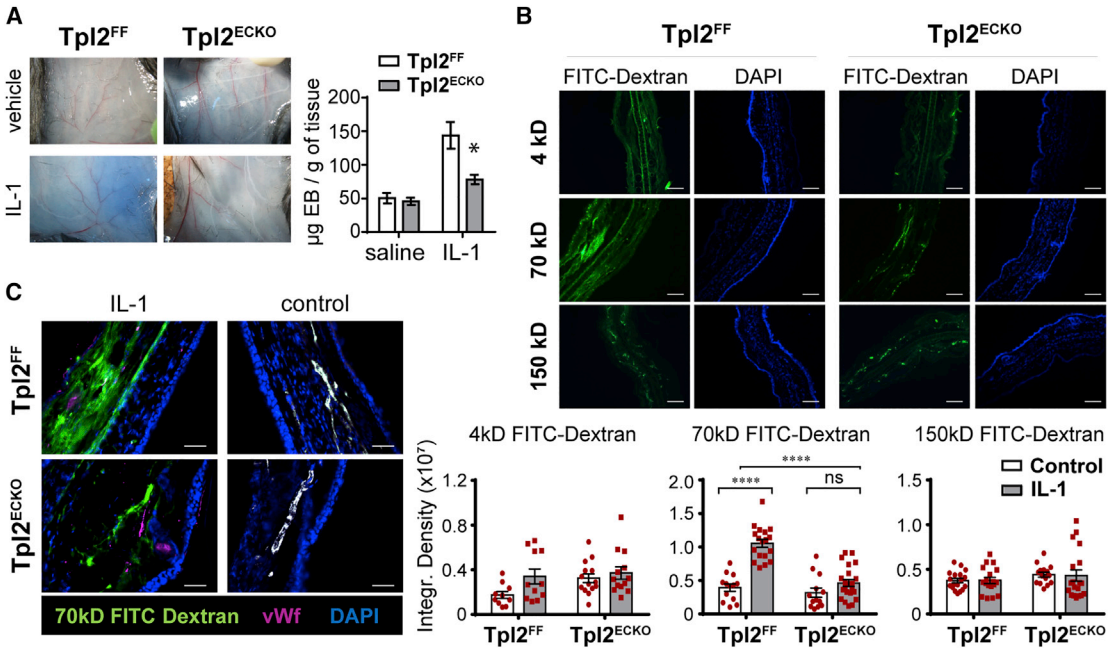

Figure 4. EC Tpl2 alters IL-1β-induced permeability *in vivo*

(A) The i.v. administration of EB in Tpl2^{FF} and Tpl2^{ECKO} mice was followed by intradermal injection of IL-1β or vehicle in the dorsal skin, 2 h after EB administration. Dye leakage was assessed 30 min later, and quantification of the extravasated EB was performed by formamide extraction from the skin corrected for tissue weight (n = 4–6 mice/genotype, unpaired two-tailed Student's t test, ±SEM).

(B) The i.v. administration of FITC-dextran 4, 70, and 150 kDa in Tpl2^{FF} and Tpl2^{ECKO} mice was followed by intradermal injection of IL-1β in the skin of right ears after either 10 min (for the 4 and 70 kDa FITC-dextran molecules) or 4 h (for the 150 kDa FITC-dextran molecule). Sections were stained with DAPI to visualize all nuclei (n = 3–5 mice per genotype and treatment; scale bar, 60 μm). Quantitation was performed by measuring the integrated density values (3–6 slides per mouse were analyzed; data represent values ± SEM, two-way ANOVA; ns, not significant).

(C) Immunohistochemistry with anti-vWf antibody for EC structures and DAPI for nuclei in control and IL-1β-treated ears after 70 kDa FITC-dextran i.v. administration (scale bars, 60 μm). The bright white staining seen in the control-treated ears indicates co-localization of anti-vWf and FITC-dextran.

Data are representative of two experiments (A–C).

increased dispersion of FITC-dextran is seen in the Tpl2^{FF} mice (Figure 4C). Finally, no changes in the diffusion of the 150 kDa FITC-dextran could be observed after IL-1β treatment in either genotype compared with the vehicle-treated ears. These results indicate that following IL-1β stimulation, endothelial Tpl2 promotes loosening of the endothelial barrier, increasing the size threshold of the passive diffusion of molecules.

To dissect the biochemical pathways associated with Tpl2 signals following inflammatory activation of ECs, primary cell cultures were used with and without IL-1β stimulation. Following IL-1β treatment of isolated lung ECs, Tpl2 deficiency attenuated JNK, p38α, and Akt phosphorylation, while phosphorylation of ERK and inhibitor κB (IκB) remained unaffected (Figures 5A and 5B). Additionally, whereas IL-1β led to the downregulation of both claudin-5 and occludin, in the absence of Tpl2 this downregulation was not observed, at least significantly for claudin-5 for both the 4 and 24 h time points (Figures 5C and 5D). To ensure the functional importance of the Tpl2-induced altered claudin-5 expression pattern, primary brain microvascular ECs (BMVECs) were isolated from Tpl2^{FF} and Tpl2^{DD} mice and treated with claudin-5 siRNA prior to IL-1β treatment (Figure 5E). *In vitro* permeability assay was performed in BMVECs by adding FITC-dextran at the top of semipermeable transwells and recording the spectrophotometric measurements of the FITC-dextran in the medium, denoting the amount of FITC-dextran that passed through the cell monolayer (Figure 5F). While Tpl2^{DD} had significantly attenuated increase in permeability compared with IL-1β-treated Tpl2^{FF} BMVECs, this difference was abolished in BMVEC cultures after treatment with claudin-5 siRNA and subsequent stimulation with IL-1β, indicating a substantial contribution of claudin-5 and a direct link between Tpl2-mediated regulation of permeability and claudin-5 levels.

As there was evidence of post-transcriptional regulation of claudin-5 by Tpl2 (Figure 2F), we then focused on claudin-5 protein turnover on primary ECs and performed rescue experiments after inhibition of protein degradation pathways. Claudin-5 has been reported to degrade through various pathways, such as through the ubiquitin-proteasome system after poly-ubiquitination of lysine 199 (Mandel et al., 2012), through lysosomal degradation (Takahashi et al., 2009), or through the activity of matrix metalloproteinase 9 (MMP9) (Chen et al., 2009). Thus, primary ECs were stimulated with IL-1β and treated with chloroquine (CQ; a lysosomal degradation inhibitor), marimastat (M; a broad metalloproteinase inhibitor), or MG132 (a proteasomal inhibitor). After analyzing the expression levels of claudin-5 and occludin through western blots, only CQ was able to increase the proteins levels of both proteins to the levels seen in Tpl2^{DD} ECs (Figure 5G). To validate that the CQ-induced claudin-5 and occludin

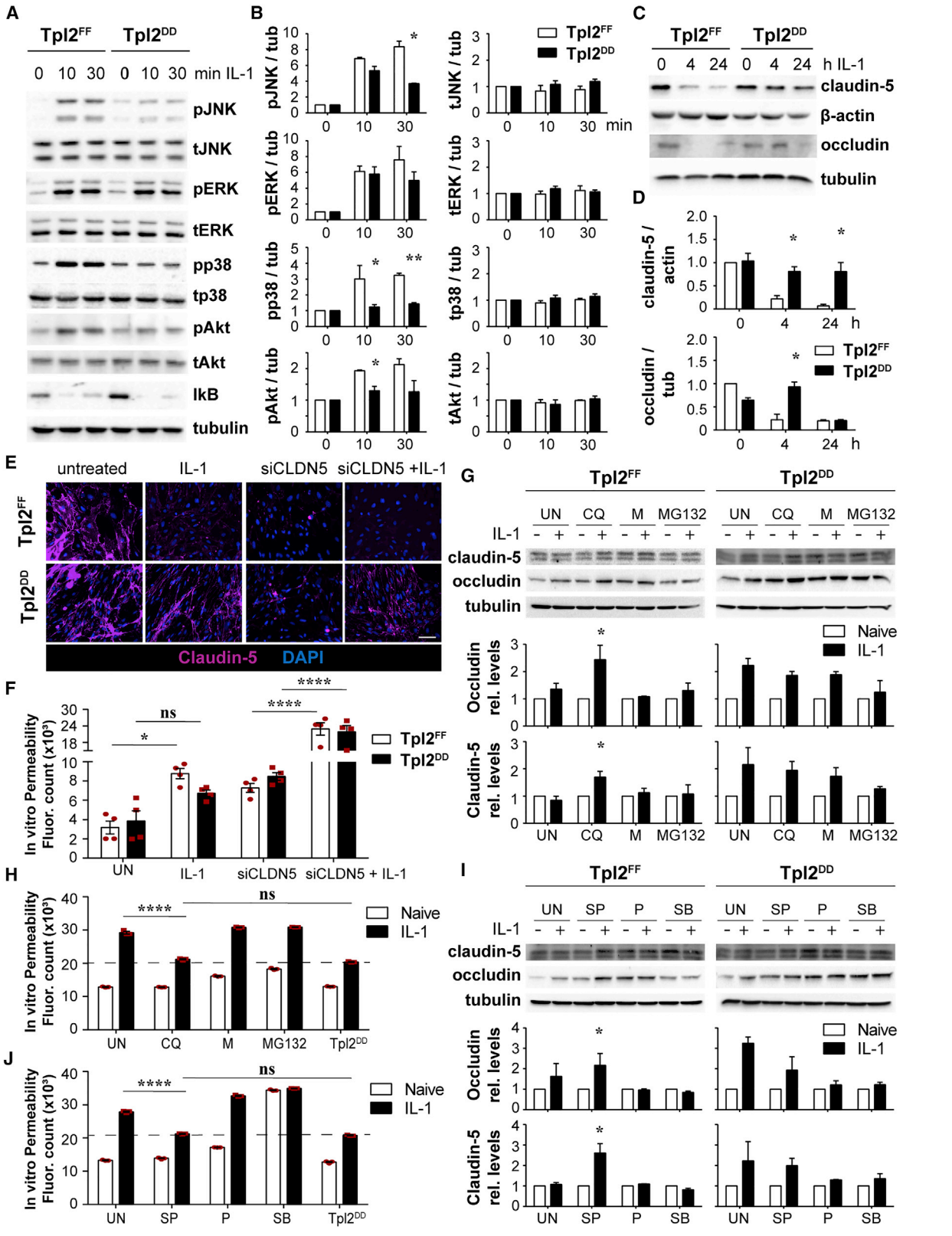

(legend on next page)

upregulation upon inflammatory stimuli had functional meaning, *in vitro* permeability assay was performed in BMVECs isolated from $Tpl2^{FF}$ and $Tpl2^{DD}$ mice (Figure 5H). Attenuation of the IL-1β-induced permeability was seen in the CQ-treated cells and restoration to the levels of the $Tpl2^{DD}$-isolated BMVECs (dashed line). Furthermore, to verify the lysosomal degradation defect in the disease context, immunofluorescence was performed in spinal cord sections of pre-symptomatic EAE mice against Lamp2 (lysosomal marker) and Rab5 (early endosomal marker). No significant differences were seen in Lamp2 staining; however, there was a significant reduction in Rab5 staining in ECs during EAE in Tpl2 absence (Figure S8). In particular, the Rab5 fluorescence intensity was measured only in ECs (signal co-localized to $CD31^+$ cells) and significant reduction was seen both in $Tpl2^{DD}$ and $Tpl2^{ECKO}$ mice, verifying a marked decrease in early endosomes. Interestingly, the early endosomal inhibition seen mirrors the EAE disease severity, as Rab5 reduction correlates to subsequent clinical score highlighting the significance of lysosomal degradation in neuroinflammation.

To elucidate the mechanism by which Tpl2 regulates claudin-5 and occludin, we then investigated the molecules altered by Tpl2 ablation. Since attenuation of JNK, p38α, and Akt phosphorylation was seen upon inflammatory stimuli, inhibitors of these signaling pathways were used to reproduce the permeability changes seen in $Tpl2^{DD}$ and $Tpl2^{ECKO}$ mice by targeting a molecule downstream of Tpl2: SP600125 (SP; inhibitor of JNK activation), perifosine (P; Akt signaling inhibitor), or SB203580 (SB; p38α signaling inhibitor). Only inhibition of JNK signaling led to the upregulation of claudin-5 and occludin upon IL-1β stimulation (Figure 5I). *In vitro* permeability assay on primary BMVECs verified that the increase seen in claudin-5 and occludin proteins resulted in reduced IL-1β-induced permeability, reaching the levels seen in $Tpl2^{DD}$ ECs (Figure 5J, dashed line).

Our results show that endothelial Tpl2 expression is required in inflamed endothelia to link inflammatory signals to the downregulation of TJ proteins through JNK signaling and the consequent TJ degradation.

Tpl2 inhibition as treatment strategy to modulate vascular permeability and tumor metastasis

To assess the translational value and therapeutic potential of our findings, we inhibited Tpl2 pharmacologically in different settings. First, a commercially available inhibitor of the Tpl2 kinase activity was used to assess its effects in an *in vivo* vascular permeability assay. Intravenous administration of Tpl2 inhibitor in wild-type mice for 4 days produced reduced permeability in the skin of the ears of experimental mice in response to intradermal IL-1β administration, as assessed by EB extravasation (Figure 6A). Second, an *in vivo* siRNA delivery system that targets specifically the lung endothelium was used (DACC lipoplex, Silence Therapeutics, Germany) (Fehring et al., 2014) to downregulate Tpl2 in the lung vasculature in the hematogenous B16Bl6 melanoma metastasis model. Mice that were inoculated intravenously with B16Bl6 cells received 2, 4, and 6 days later DACC/siRNATpl2 or DACC/siRNALuc lipoplex (expressing a non-targeting control siRNA). Metastatic nodule formation was assessed 12 days post tumor cell inoculation, and stereoscopic examination of the lungs showed that EC-specific Tpl2 siRNA treatment reduced significantly the number of tumor nodules compared with mice treated with sucrose or luciferase siRNA. This reduction in tumor formation was associated with reduced numbers of infiltrating T and B cells, as seen after H&E staining (Figures 6B and 6C). Moreover, staining and quantification of the TJ protein claudin-5 revealed significantly increased protein expression in the Tpl2 siRNA-treated mice in comparison with controls (Figures 6D and 6E). Further histological analysis confirmed the successful downregulation of Tpl2 protein in the lung endothelial structures and revealed no differences between treatments in lung vessel architecture or pericyte coverage (Figure S9).

Figure 5. EC Tpl2 alters inflammatory signaling, expression of barrier-associated molecules, and IL-1β-induced permeability *in vitro*

(A) Cultured ECs from $Tpl2^{FF}$ and $Tpl2^{DD}$ mice were treated with IL-1β for 0, 15, and 30 min. Cell lysates were subjected to western blot analysis against both phosphorylated and total JNK, ERK, p38, and Akt, as well as total IκB and tubulin.

(B) Densitometric analysis was performed using Image Lab, and all values were normalized to tubulin values (n = 2–3 per genotype/condition, unpaired two-tailed Student's t test, ±SEM).

(C) Cultured ECs from $Tpl2^{FF}$ and $Tpl2^{DD}$ mice were treated with IL-1β for 0, 4, and 24 h. Cell lysates were subjected to western blot analysis against claudin-5, occludin, β-actin, and tubulin.

(D) Densitometric analysis was performed for the quantification of claudin-5 relative to β-actin and of occludin relative to tubulin (n = 2 per genotype/condition, unpaired one-tailed Student's t test, ±SEM).

(E) Primary brain microvascular ECs (BMVECs) from $Tpl2^{FF}$ and $Tpl2^{DD}$ mice treated with vesicle, siRNA against claudin-5 (CLD5), or non-translating (NT) siRNA for 72 h and IL-1β for 24 h. Immunofluorescence of BVMEC cultures was performed for claudin-5 and nuclei (DAPI) 24 h after IL-1β treatment (scale bar, 30 μm).

(F) *In vitro* permeability assay was then performed by adding FITC-dextran (70 kDa molecule) for 60 min and measuring spectrophotometrically the FITC-dextran passing through the monolayer into medium (two-way ANOVA with Tukey's multiple comparisons test, ±SEM).

(G and I) Cultured ECs from $Tpl2^{FF}$ and $Tpl2^{DD}$ mice were treated with IL-1β for 30 h in total, and 6 h after administration, inhibitors were added to the cells: chloroquine (CQ), marimastat (M), and MG132 (G) or SP600125 (SP; inhibitor of JNK activation), perifosine (P; Akt signaling inhibitor), and SB203580 (SB; p38α signaling inhibitor) (I). Cell lysates were subjected to western blot analysis against claudin-5, occludin, and tubulin. Densitometric analysis was performed using Image Lab, and all values were normalized to tubulin values (n = 2–3 per genotype/condition, unpaired two-tailed Student's t test, ±SEM).

(H and J) Cultured ECs from $Tpl2^{FF}$ were treated with IL-1β for 30 h in total, and 6 h after administration, inhibitors (CQ, M, or MG132) were added to the cells: CQ, M, and MG132 (H), or SP, P, and SB (J). ECs from $Tpl2^{DD}$ mice were treated only with IL-1β for 30 h. FITC-dextran (70 kDa molecule) was added after the treatment for 60 min, and spectrophotometric measurement of the dextran passing through the monolayer was assessed in medium (two-way ANOVA with Tukey's multiple comparisons test, ±SEM). When comparing all conditions before (naive) and after IL-1β administration, significance was reached (****) independent of treatment, except after SB treatment where no statistical significance was observed between naive and IL-1β-induced levels (J); stars were omitted for simplicity.

Data are representative of two experiments (A, C, H, and J) or average values of two experiments (B, D, E, F, G, and H).

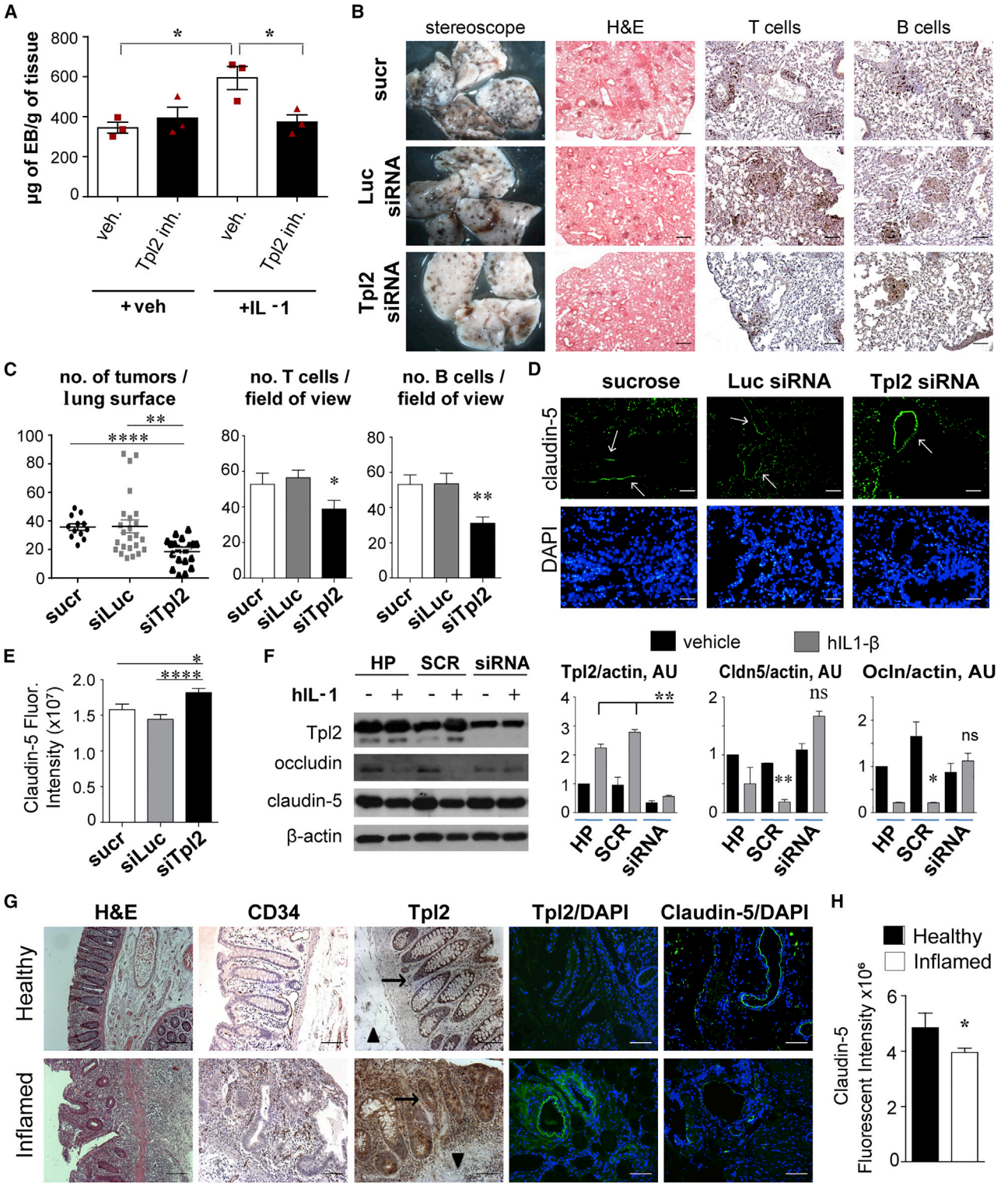

Figure 6. Tpl2 inhibition as a therapeutic strategy in vascular-permeability-associated inflammatory conditions

(A) The i.v. administration of Tpl2 inhibitor or saline performed for 4 days in Tpl2^{FF} mice. Mice were then injected with EB followed by intradermal injection of IL-1β in the ears. Extravasated EB was measured through spectrophotometry (n = 4 mice/treatment; one-way ANOVA with Tukey's multiple comparisons test, ±SEM).

(legend continued on next page)

Finally, to determine whether the aforementioned endothelial-specific function of Tpl2 applies also in human conditions, Tpl2 expression and function were analyzed in human brain microvascular ECs (HBMVECs). HBMVECs expressed high levels of Tpl2 and downregulated both claudin-5 and occludin in response to hIL-1β treatment. Treatment with Tpl2 siRNA led to significant partial downregulation of Tpl2 expression and resulted in the rescue of endothelial claudin-5 and occludin downregulation produced by IL-1β (Figure 6F). Furthermore, the Tpl2 expression pattern was assessed in human inflammatory tissue showing an association between increased Tpl2 and decreased claudin-5 expression. In particular, significantly enhanced Tpl2 staining was observed in inflammatory cells at inflamed human colon samples compared with healthy colon samples and also on ECs of the inflamed vasculature in the mucosa (villi) and submucosa area of colons (Figure 6G). There was increased Tpl2 expression in inflammatory vessels, especially in the submucosa area, where there was less destruction and EC structures were clearly visible during inflammation compared with the villi. This was correlated with significantly reduced claudin-5 expression in endothelia, as seen by immunohistochemistry and integrated fluorescent density measurements in colon specimens (Figures 6G and 6H).

Thus, endothelium-targeted siRNA or small molecule inhibition of Tpl2 function may be of clinical value for the treatment of a range of vascular-permeability-associated diseases, and it could have a cumulative effect for disease management in conjunction to its inhibition in inflammatory cells.

DISCUSSION

The current study demonstrates a key role for the Tpl2 kinase in controlling vascular permeability of ECs in inflammation. Although the proinflammatory function of Tpl2 through inflammatory mediators is well documented (Xu et al., 2018), here we show that endothelial Tpl2 signaling plays an important proinflammatory and endothelial regulatory role in various models of inflammation and cancer metastasis in which the endothelium is heavily involved.

We have previously shown that Tpl2 signaling in radiation-resistant stromal cells regulated both the onset and severity of EAE (Sriskantharajah et al., 2014). Here, we have identified that EC-specific Tpl2 deletion recapitulated the phenotype seen in complete Tpl2-deleted EAE mice, whereas no differences were seen in microglial-, astrocytic-, or neuronal-specific Tpl2 deletion. In particular, EC-specific and completely Tpl2-deleted mice presented similar demyelination, immune cell infiltration, and BBB dysfunction, as assessed by albumin and fibrinogen leakage, which are considered biomarkers of BBB breakdown, exacerbation of demyelination/inflammation, and inhibition of repair (Alvarez et al., 2011; Ryu et al., 2015; Schachtrup et al., 2007). Furthermore, *in vivo* assessment of spinal cord permeability through different assays confirmed that Tpl2 deficiency in ECs reduced vascular permeability, and this reduction was correlated with altered expression of TJ proteins claudin-5 and occludin. Downregulation of claudin-5 and occludin has been correlated with BBB breakdown in EAE (Argaw et al., 2009), and claudin-5-deficient mice have size-selective BBB opening and die prematurely (Nitta et al., 2003), suggesting that Tpl2-mediated maintenance of claudin-5 expression could prevent BBB disruption. Similarly, occludin has been shown to correlate with TJ formation, to regulate junction permeability (Hirase et al., 2001), and to exhibit altered expression in the spinal cord after EAE induction (Kebir et al., 2007). Thus, our data indicate that endothelial Tpl2 is important for TJ-mediated regulation of permeability in the CNS, especially when taking into account that cellular adhesion and angiogenic EC properties remained unaltered. The importance of this finding is highlighted by the fact that several CNS disorders have been associated with BBB breakdown, such as Alzheimer's and Parkinson's diseases, stroke, amyotrophic lateral sclerosis, and brain tumors (Sweeney et al., 2018), as well as with claudin-5 downregulation, such as glioblastoma multiforme (Liebner et al., 2000), amyotrophic lateral sclerosis (Zhong et al., 2008), and viral encephalomyelitis (Gralinski et al., 2009).

Proinflammatory mediators have dramatic effects on EC function altering vascular tone, endothelial permeability, and leukocyte/malignant cell diapedesis. Cancer cell extravasation in tumor progression and blood-borne metastasis to secondary sites resembles the process of leukocyte recruitment during inflammation and involves similar cellular mechanisms (Neri and Bicknell, 2005; Strell and Entschladen, 2008). Since the interaction between the ECs and tumor cells, as well as the penetration of tumor cells through TJs and AJs, is a key event in the establishment of metastasis (Martin and Jiang, 2009), we have also assessed the role of endothelial Tpl2 in a model of tumor growth and hematogenous metastasis. Endothelial Tpl2 deletion significantly reduced the metastatic burden, reduced

(B and C) B16Bl6 melanoma cells were i.v. transferred to C57BL/6 mice along with sucrose, luciferase siRNA, or Tpl2 siRNA. Mice were sacrificed 12 dpi, and images of mouse lungs were taken in the stereoscope. Lung sections were stained for H&E and with antibodies against CD3 and B220. Scale bars: 150 μm for H&E and 60 μm for CD3 and B220.

(C) Quantification of tumors per lung surface was performed as well as quantification of the number of T and B cells per field of view (unpaired two-tailed Student's t test, ±SEM).

(D and E) Representative lung immunohistochemistry against claudin-5 and nuclei was performed and quantification of integrated density of protein fluorescent intensity for claudin-5 (n = 5–8 mice/treatment, >20 field of view/treatment; scale bar, 30 μm). Arrows show vascular structures.

(F) Human brain microvascular endothelial cells (HBMVCs) were analyzed by western blot analysis after treatment with Tpl2 siRNA or controls (HiPerfect transfection reagent vehicle control [HP] or scramble siRNA [SCR]) for 72 h, and hIL-1β for the last 24 h. IL-1β-treated siRNA cells were compared with HP/SCR-treated cells for Tpl2 analysis, and untreated cells were compared with IL-1β-treated SCR/Tpl2 siRNA cells for occludin and claudin-5 analysis (unpaired two-tailed Student's t test, ±SEM; ns, not significant).

(G and H) Imaging of inflammation (H&E), vasculature (CD34), Tpl2, claudin-5, and nuclei in healthy and inflamed human colon samples (n = 5 subjects/group; scale bar, 60 μm). Arrows indicate colon mucosa, and arrowheads indicate the submucosa areas. Quantification of claudin-5-intergraded fluorescent intensity (H) was performed (mean fluorescence intensity ± SEM, unpaired two-tailed Student's t test; 10 fields of view per sample, 5 samples per group).

Data are representative of two independent experiments (A, B, and D–F) or average values of two experiments (C).

inflammatory cell infiltration, and contributed to undiminished claudin-5 and ZO-1 protein expression. Although the significant, albeit modest, effect of Tpl2 ablation on TJ protein downregulation might not exclusively account for the observed phenotype, it was consistently present and could possibly get amplified to a greater downstream molecular divergence. Considering that enhancement of vascular endothelial barrier protects from cancer cell extravasation (Criscuoli et al., 2005) and that altered expression of TJs is associated with different types of human cancer metastasis (Huang et al., 2011; Martin and Jiang, 2009), targeting endothelial Tpl2 could provide a viable future therapeutic strategy.

Biochemically, IL-1β treatment of Tpl2-deficient ECs led to reduced JNK, p38, and Akt kinase activation and attenuated downregulation of TJ proteins, with no effect on ERK. Although Tpl2 signaling has been linked to ERK regulation, tissue-dependent signaling can adequately explain the unaltered ERK phosphorylation in ECs after Tpl2 ablation (Das et al., 2005). Although all the affected kinases have been previously associated with endothelial barrier permeability (Kilic et al., 2006; Li et al., 2015; Liu et al., 2014), we identified that only inhibition of JNK signaling could recapitulate the vascular permeability seen in the $Tpl2^{ECKO}$ mice. Such a finding is supported by reports of increased BBB permeability after white matter injury due to JNK activation (Wang et al., 2012), as well as reports of restoration of the reduced claudin-5 expression in a rat model of subarachnoid hemorrhage upon JNK signaling inhibition (Chen et al., 2012). In addition, we also showed that inhibition of the lysosomal degradation pathway had similar effect to the inhibition of JNK signaling, as it increased the protein levels of both claudin-5 and occludin, as well as decreased the IL-1β-induced permeability of ECs. EC-specific lysosomal degradation defect was also validated in a disease context, as pre-symptomatic EAE mice showed a marked decrease in early endosome formation in the absence of Tpl2. Taken together in conjunction to the fact that activation of lysosomal degradation has been linked to JNK signaling (Lorin et al., 2010; Sui et al., 2014), a signaling cascade is suggested where inhibition of JNK signaling blocks the activation of lysosomal degradation that, in turn, prevents the downregulation of claudin-5 and occludin in response to inflammatory stimuli and decreases the inflammation-induced vascular permeability.

Interestingly, a report has identified a correlation of high Tpl2 expression to increased incidence of distant metastasis in human colorectal cancer patients (Pyo et al., 2018). Furthermore, pharmacological or gene-silencing-mediated Tpl2 inhibition reduced tumor angiogenesis in a mouse model of peritoneal dissemination, suggesting Tpl2 inhibition as a valid therapeutic approach for preventing tumor dissemination (Lee et al., 2013). To assess the pharmacological potential of Tpl2 inhibition, we investigated EC-specific Tpl2 RNA interference as a therapeutic intervention. Interestingly, this approach reversed the altered TJ protein expression upon IL-1β stimulation and endothelial permeability *in vitro* and *in vivo*, as well as reduced significantly the tumor burden. To validate our findings in human samples, we studied Tpl2 expression in human inflamed colon. The importance of the stromal-cell-specific function of Tpl2 has been demonstrated in both Crohn's disease and colitis-associated tumorigenesis, where signaling of Tpl2 in intestinal myofibroblasts is crucial for injury and homeostatic responses (Koliaraki et al., 2012; Roulis et al., 2014). Here, Tpl2 overexpression was identified in vascular structures in inflamed human colon samples in comparison with healthy colon samples, and concomitant reduction of claudin-5 expression was also observed. These findings, coupled with the fact the Tpl2 is expressed in human ECs and regulates TJ proteins, underline the therapeutic implications of Tpl2 signaling in ECs and provide context in its association to metastatic events.

Despite the well-documented proinflammatory activities of Tpl2, Tpl2 deficiency was recently shown to also increase inflammation in mouse models of allergic airway inflammation and dextran sulfate sodium (DSS) colitis, and such an increase was attributed to A20-binding inhibitor of NFκB 2 (ABIN-2) loss, a component of the Tpl2 complex, which requires Tpl2 for stability (Nanda et al., 2018; Ventura et al., 2018). Nonetheless, in EAE, we have shown previously that reduced catalytic activity of Tpl2 is essential for protection against the disease and independent of ABIN-2 expression and Tpl2's adaptor function (Sriskantharajah et al., 2014). Taken into account that treatment with Tpl2 inhibitor exhibited a protective effect against metastatic nodules, it is likely that inhibition of Tpl2 activity rather than its ABIN-2 adaptor function is needed for metastasis protection, although more studies are needed to elucidate the exact mechanism. Nonetheless, in the two inflammation models tested here, endothelial Tpl2 deletion reduced vascular permeability, at least partly, through TJ proteins, and more importantly, it reduced the IL-1β-mediated increase in EC permeability. This effect was abolished after treatment with claudin-5 siRNA highlighting a potential direct link between Tpl2-mediated regulation of permeability and claudin-5 protein expression. This is also supported by a study reporting disease suppression after Tpl2 inhibition in a model of diabetic retinopathy, which is characterized by microvascular complications, vascular leakage, inflammation, and BBB breakdown (Lai et al., 2017).

Therefore, development of small molecule inhibitors targeting either Tpl2 or Tpl2 downstream targets blocking its signaling in inflamed endothelia could be effective in the treatment of a diverse range of diseases associated with defects in inflammation-induced barrier permeability. More importantly, such therapeutic interventions could be developed in conjunction with the already reported anti-inflammatory effects of Tpl2 inhibition in the lymphocytic compartment, providing a thorough and integrated strategy against acute and chronic inflammatory diseases.

STAR★METHODS

Detailed methods are provided in the online version of this paper and include the following:

- KEY RESOURCES TABLE
- RESOURCE AVAILABILITY
  - Lead contact
  - Materials availability
  - Data and code availability

SUPPLEMENTAL INFORMATION

Supplemental information can be found online at https://doi.org/10.1016/j.celrep.2021.109168.

ACKNOWLEDGMENTS

We thank Marilena Manolika for excellent technical assistance and mouse genotyping and Niki Tsakiri for experimental work. We also thank Spiros Lalos, Anna Katevaini, Lida Iliopoulou, and Panagiotis Athanasakis for technical assistance, as well as Sofia Grammenoudi for flow cytometry support. The graphical abstract was created using BioRender.com. This work was supported by FP7 Advanced ERC Grant MCs-inTEST (grant agreement no. 340217) to G.K. The authors also wish to thank the InfrafrontierGR Infrastructure (co-funded by Greece and the European Union [European Regional Development Fund] under NSRF 2014–2020 [MIS 5002135]) for providing mouse hosting and phenotyping facilities, including transgenesis, histopathology, flow cytometry, and advanced microscopy facilities.

AUTHOR CONTRIBUTIONS

Conceptualization, G.K.; methodology, A.N., S.L., and G.K.; investigation, A.N., M.B., and S.L.; resources, S.V., U.S., and S.L.; writing – original draft, A.N.; writing – review & editing, A.N., G.K., and S.L.; funding acquisition, G.K.; supervision, G.K.

DECLARATION OF INTERESTS

Ute Schaeper is employed by Silence Therapeutics GmbH. All other authors declare no competing interests.

Received: July 10, 2019
Revised: April 8, 2021
Accepted: May 3, 2021
Published: May 25, 2021

REFERENCES

Alvarez, J.I., Dodelet-Devillers, A., Kebir, H., Ifergan, I., Fabre, P.J., Terouz, S., Sabbagh, M., Wosik, K., Bourbonniere, L., Bernard, M., et al. (2011). The Hedgehog pathway promotes blood-brain barrier integrity and CNS immune quiescence. Science *334*, 1727–1731.

Argaw, A.T., Gurfein, B.T., Zhang, Y., Zameer, A., and John, G.R. (2009). VEGF-mediated disruption of endothelial CLN-5 promotes blood-brain barrier breakdown. Proc. Natl. Acad. Sci. USA *106*, 1977–1982.

Boillée, S., Yamanaka, K., Lobsiger, C.S., Copeland, N.G., Jenkins, N.A., Kassiotis, G., Kollias, G., and Cleveland, D.W. (2006). Onset and progression in inherited ALS determined by motor neurons and microglia. Science *312*, 1389–1392.

Chen, F., Ohashi, N., Li, W., Eckman, C., and Nguyen, J.H. (2009). Disruptions of occludin and claudin-5 in brain endothelial cells in vitro and in brains of mice with acute liver failure. Hepatology *50*, 1914–1923.

Chen, D., Wei, X.T., Guan, J.H., Yuan, J.W., Peng, Y.T., Song, L., and Liu, Y.H. (2012). Inhibition of c-Jun N-terminal kinase prevents blood-brain barrier disruption and normalizes the expression of tight junction proteins claudin-5 and ZO-1 in a rat model of subarachnoid hemorrhage. Acta Neurochir. (Wien) *154*, 1469–1476, discussion 1476.

Clark, A.M., Reynolds, S.H., Anderson, M., and Wiest, J.S. (2004). Mutational activation of the MAP3K8 protooncogene in lung cancer. Genes Chromosomes Cancer *41*, 99–108.

Coisne, C., Dehouck, L., Faveeuw, C., Delplace, Y., Miller, F., Landry, C., Morissette, C., Fenart, L., Cecchelli, R., Tremblay, P., and Dehouck, B. (2005). Mouse syngenic in vitro blood-brain barrier model: a new tool to examine inflammatory events in cerebral endothelium. Lab. Invest. *85*, 734–746.

Criscuoli, M.L., Nguyen, M., and Eliceiri, B.P. (2005). Tumor metastasis but not tumor growth is dependent on Src-mediated vascular permeability. Blood *105*, 1508–1514.

Das, S., Cho, J., Lambertz, I., Kelliher, M.A., Eliopoulos, A.G., Du, K., and Tsichlis, P.N. (2005). Tpl2/cot signals activate ERK, JNK, and NF-kappaB in a cell-type and stimulus-specific manner. J. Biol. Chem. *280*, 23748–23757.

Dumitru, C.D., Ceci, J.D., Tsatsanis, C., Kontoyiannis, D., Stamatakis, K., Lin, J.H., Patriotis, C., Jenkins, N.A., Copeland, N.G., Kollias, G., and Tsichlis, P.N. (2000). TNF-alpha induction by LPS is regulated posttranscriptionally via a Tpl2/ERK-dependent pathway. Cell *103*, 1071–1083.

Eliopoulos, A.G., Dumitru, C.D., Wang, C.C., Cho, J., and Tsichlis, P.N. (2002). Induction of COX-2 by LPS in macrophages is regulated by Tpl2-dependent CREB activation signals. EMBO J. *21*, 4831–4840.

Fehring, V., Schaeper, U., Ahrens, K., Santel, A., Keil, O., Eisermann, M., Giese, K., and Kaufmann, J. (2014). Delivery of therapeutic siRNA to the lung endothelium via novel Lipoplex formulation DACC. Mol. Ther. *22*, 811–820.

Gantke, T., Sriskantharajah, S., Sadowski, M., and Ley, S.C. (2012). IκB kinase regulation of the TPL-2/ERK MAPK pathway. Immunol. Rev. *246*, 168–182.

Gralinski, L.E., Ashley, S.L., Dixon, S.D., and Spindler, K.R. (2009). Mouse adenovirus type 1-induced breakdown of the blood-brain barrier. J. Virol. *83*, 9398–9410.

Groeneveld, A.B.J. (2002). Vascular pharmacology of acute lung injury and acute respiratory distress syndrome. Vascul. Pharmacol. *39*, 247–256.

Gustafsson, E., Brakebusch, C., Hietanen, K., and Fässler, R. (2001). Tie-1-directed expression of Cre recombinase in endothelial cells of embryoid bodies and transgenic mice. J. Cell Sci. *114*, 671–676.

Hawkins, B.T., and Davis, T.P. (2005). The blood-brain barrier/neurovascular unit in health and disease. Pharmacol. Rev. *57*, 173–185.

Hirase, T., Kawashima, S., Wong, E.Y., Ueyama, T., Rikitake, Y., Tsukita, S., Yokoyama, M., and Staddon, J.M. (2001). Regulation of tight junction permeability and occludin phosphorylation by Rhoa-p160ROCK-dependent and -independent mechanisms. J. Biol. Chem. *276*, 10423–10431.

Huang, R.L., Teo, Z., Chong, H.C., Zhu, P., Tan, M.J., Tan, C.K., Lam, C.R., Sng, M.K., Leong, D.T., Tan, S.M., et al. (2011). ANGPTL4 modulates vascular junction integrity by integrin signaling and disruption of intercellular VE-cadherin and claudin-5 clusters. Blood *118*, 3990–4002.

Kaiser, F., Cook, D., Papoutsopoulou, S., Rajsbaum, R., Wu, X., Yang, H.T., Grant, S., Ricciardi-Castagnoli, P., Tsichlis, P.N., Ley, S.C., and O'Garra, A. (2009). TPL-2 negatively regulates interferon-beta production in macrophages and myeloid dendritic cells. J. Exp. Med. *206*, 1863–1871.

Kebir, H., Kreymborg, K., Ifergan, I., Dodelet-Devillers, A., Cayrol, R., Bernard, M., Giuliani, F., Arbour, N., Becher, B., and Prat, A. (2007). Human TH17 lymphocytes promote blood-brain barrier disruption and central nervous system inflammation. Nat. Med. *13*, 1173–1175.

Kilic, E., Kilic, U., Wang, Y., Bassetti, C.L., Marti, H.H., and Hermann, D.M. (2006). The phosphatidylinositol-3 kinase/Akt pathway mediates VEGF's neuroprotective activity and induces blood brain barrier permeability after focal cerebral ischemia. FASEB J. *20*, 1185–1187.

Koliaraki, V., Roulis, M., and Kollias, G. (2012). Tpl2 regulates intestinal myofibroblast HGF release to suppress colitis-associated tumorigenesis. J. Clin. Invest. *122*, 4231–4242.

Lai, D.W., Lin, K.H., Sheu, W.H., Lee, M.R., Chen, C.Y., Lee, W.J., Hung, Y.W., Shen, C.C., Chung, T.J., Liu, S.H., and Sheu, M.L. (2017). TPL2 (Therapeutic Targeting Tumor Progression Locus-2)/ATF4 (Activating Transcription Factor-4)/SDF1α (Chemokine Stromal Cell-Derived Factor-α) Axis Suppresses Diabetic Retinopathy. Circ. Res. *121*, e37–e52.

Lakso, M., Pichel, J.G., Gorman, J.R., Sauer, B., Okamoto, Y., Lee, E., Alt, F.W., and Westphal, H. (1996). Efficient in vivo manipulation of mouse genomic sequences at the zygote stage. Proc. Natl. Acad. Sci. USA *93*, 5860–5865.

Lassmann, H., Suchanek, G., and Ozawa, K. (1994). Histopathology and the blood-cerebrospinal fluid barrier in multiple sclerosis. Ann. Neurol. *36* (*Suppl*), S42–S46.

Lee, W.J., Lan, K.H., Chou, C.T., Yi, Y.C., Chen, W.C., Pan, H.C., Peng, Y.C., Wang, K.B., Chen, Y.C., Chao, T.H., et al. (2013). Tpl2 inhibitors thwart endothelial cell function in angiogenesis and peritoneal dissemination. Neoplasia *15*, 1036–1048.

Lee, H.W., Choi, H.Y., Joo, K.M., and Nam, D.H. (2015). Tumor progression locus 2 (Tpl2) kinase as a novel therapeutic target for cancer: double-sided effects of Tpl2 on cancer. Int. J. Mol. Sci. *16*, 4471–4491.

Li, L., Hu, J., He, T., Zhang, Q., Yang, X., Lan, X., Zhang, D., Mei, H., Chen, B., and Huang, Y. (2015). P38/MAPK contributes to endothelial barrier dysfunction via MAP4 phosphorylation-dependent microtubule disassembly in inflammation-induced acute lung injury. Sci. Rep. *5*, 8895.

Liebner, S., Fischmann, A., Rascher, G., Duffner, F., Grote, E.H., Kalbacher, H., and Wolburg, H. (2000). Claudin-1 and claudin-5 expression and tight junction morphology are altered in blood vessels of human glioblastoma multiforme. Acta Neuropathol. *100*, 323–331.

Liu, X., Zhou, X., and Yuan, W. (2014). The angiopoietin1-Akt pathway regulates barrier function of the cultured spinal cord microvascular endothelial cells through Eps8. Exp. Cell Res. *328*, 118–131.

Lorin, S., Pierron, G., Ryan, K.M., Codogno, P., and Djavaheri-Mergny, M. (2010). Evidence for the interplay between JNK and p53-DRAM signalling pathways in the regulation of autophagy. Autophagy *6*, 153–154.

Mandel, I., Paperna, T., Volkowich, A., Merhav, M., Glass-Marmor, L., and Miller, A. (2012). The ubiquitin-proteasome pathway regulates claudin 5 degradation. J. Cell. Biochem. *113*, 2415–2423.

Martin, T.A., and Jiang, W.G. (2009). Loss of tight junction barrier function and its role in cancer metastasis. Biochim. Biophys. Acta *1788*, 872–891.

McNab, F.W., Ewbank, J., Rajsbaum, R., Stavropoulos, E., Martirosyan, A., Redford, P.S., Wu, X., Graham, C.M., Saraiva, M., Tsichlis, P., et al. (2013). TPL-2-ERK1/2 signaling promotes host resistance against intracellular bacterial infection by negative regulation of type I IFN production. J. Immunol. *191*, 1732–1743.

Mierke, C.T., Zitterbart, D.P., Kollmannsberger, P., Raupach, C., Schlötzer-Schrehardt, U., Goecke, T.W., Behrens, J., and Fabry, B. (2008). Breakdown of the endothelial barrier function in tumor cell transmigration. Biophys. J. *94*, 2832–2846.

Nanda, S.K., Nagamori, T., Windheim, M., Amu, S., Aviello, G., Patterson-Kane, J., Arthur, J.S.C., Ley, S.C., Fallon, P., and Cohen, P. (2018). ABIN2 Function Is Required To Suppress DSS-Induced Colitis by a Tpl2-Independent Mechanism. J. Immunol. *201*, 3373–3382.

Neri, D., and Bicknell, R. (2005). Tumour vascular targeting. Nat. Rev. Cancer *5*, 436–446.

Newman, S., Fan, L., Pribnow, A., Silkov, A., Rice, S.V., Lee, S., Shao, Y., Shaner, B., Mulder, H., Nakitandwe, J., et al. (2019). Clinical genome sequencing uncovers potentially targetable truncations and fusions of MAP3K8 in spitzoid and other melanomas. Nat. Med. *25*, 597–602.

Nitta, T., Hata, M., Gotoh, S., Seo, Y., Sasaki, H., Hashimoto, N., Furuse, M., and Tsukita, S. (2003). Size-selective loosening of the blood-brain barrier in claudin-5-deficient mice. J. Cell Biol. *161*, 653–660.

Obermeier, B., Daneman, R., and Ransohoff, R.M. (2013). Development, maintenance and disruption of the blood-brain barrier. Nat. Med. *19*, 1584–1596.

Papoutsopoulou, S., Symons, A., Tharmalingham, T., Belich, M.P., Kaiser, F., Kioussis, D., O'Garra, A., Tybulewicz, V., and Ley, S.C. (2006). ABIN-2 is required for optimal activation of Erk MAP kinase in innate immune responses. Nat. Immunol. *7*, 606–615.

Pattison, M.J., Mitchell, O., Flynn, H.R., Chen, C.S., Yang, H.T., Ben-Addi, H., Boeing, S., Snijders, A.P., and Ley, S.C. (2016). TLR and TNF-R1 activation of the MKK3/MKK6-p38α axis in macrophages is mediated by TPL-2 kinase. Biochem. J. *473*, 2845–2861.

Pyo, J.S., Park, M.J., and Kim, C.N. (2018). TPL2 expression is correlated with distant metastasis and poor prognosis in colorectal cancer. Hum. Pathol. *79*, 50–56.

Rothhammer, V., Heink, S., Petermann, F., Srivastava, R., Claussen, M.C., Hemmer, B., and Korn, T. (2011). Th17 lymphocytes traffic to the central nervous system independently of α4 integrin expression during EAE. J. Exp. Med. *208*, 2465–2476.

Roulis, M., Nikolaou, C., Kotsaki, E., Kaffe, E., Karagianni, N., Koliaraki, V., Salpea, K., Ragoussis, J., Aidinis, V., Martini, E., et al. (2014). Intestinal myofibroblast-specific Tpl2-Cox-2-PGE2 pathway links innate sensing to epithelial homeostasis. Proc. Natl. Acad. Sci. USA *111*, E4658–E4667.

Rubin, L.L., and Staddon, J.M. (1999). The cell biology of the blood-brain barrier. Annu. Rev. Neurosci. *22*, 11–28.

Ryu, J.K., Petersen, M.A., Murray, S.G., Baeten, K.M., Meyer-Franke, A., Chan, J.P., Vagena, E., Bedard, C., Machado, M.R., Rios Coronado, P.E., et al. (2015). Blood coagulation protein fibrinogen promotes autoimmunity and demyelination via chemokine release and antigen presentation. Nat. Commun. *6*, 8164.

Schachtrup, C., Lu, P., Jones, L.L., Lee, J.K., Lu, J., Sachs, B.D., Zheng, B., and Akassoglou, K. (2007). Fibrinogen inhibits neurite outgrowth via beta 3 integrin-mediated phosphorylation of the EGF receptor. Proc. Natl. Acad. Sci. USA *104*, 11814–11819.

Shiels, I.A., Zhang, S., Ambler, J., and Taylor, S.M. (1998). Vascular leakage stimulates phenotype alteration in ocular cells, contributing to the pathology of proliferative vitreoretinopathy. Med. Hypotheses *50*, 113–117.

Sriskantharajah, S., Gückel, E., Tsakiri, N., Kierdorf, K., Brender, C., Ben-Addi, A., Veldhoen, M., Tsichlis, P.N., Stockinger, B., O'Garra, A., et al. (2014). Regulation of experimental autoimmune encephalomyelitis by TPL-2 kinase. J. Immunol. *192*, 3518–3529.

Stamatovic, S.M., Keep, R.F., and Andjelkovic, A.V. (2008). Brain endothelial cell-cell junctions: how to "open" the blood brain barrier. Curr. Neuropharmacol. *6*, 179–192.

Strell, C., and Entschladen, F. (2008). Extravasation of leukocytes in comparison to tumor cells. Cell Commun. Signal. *6*, 10.

Sui, X., Kong, N., Ye, L., Han, W., Zhou, J., Zhang, Q., He, C., and Pan, H. (2014). p38 and JNK MAPK pathways control the balance of apoptosis and autophagy in response to chemotherapeutic agents. Cancer Lett. *344*, 174–179.

Sweeney, M.D., Sagare, A.P., and Zlokovic, B.V. (2018). Blood-brain barrier breakdown in Alzheimer disease and other neurodegenerative disorders. Nat. Rev. Neurol. *14*, 133–150.

Takahashi, S., Iwamoto, N., Sasaki, H., Ohashi, M., Oda, Y., Tsukita, S., and Furuse, M. (2009). The E3 ubiquitin ligase LNX1p80 promotes the removal of claudins from tight junctions in MDCK cells. J. Cell Sci. *122*, 985–994.

Tomczak, M.F., Gadjeva, M., Wang, Y.Y., Brown, K., Maroulakou, I., Tsichlis, P.N., Erdman, S.E., Fox, J.G., and Horwitz, B.H. (2006). Defective activation of

ERK in macrophages lacking the p50/p105 subunit of NF-kappaB is responsible for elevated expression of IL-12 p40 observed after challenge with Helicobacter hepaticus. J. Immunol. *176*, 1244–1251.

Ventura, S., Cano, F., Kannan, Y., Breyer, F., Pattison, M.J., Wilson, M.S., and Ley, S.C. (2018). A20-binding inhibitor of NF-κB (ABIN) 2 negatively regulates allergic airway inflammation. J. Exp. Med. *215*, 2737–2747.

Vougioukalaki, M., Kanellis, D.C., Gkouskou, K., and Eliopoulos, A.G. (2011). Tpl2 kinase signal transduction in inflammation and cancer. Cancer Lett. *304*, 80–89.

Wang, L.W., Tu, Y.F., Huang, C.C., and Ho, C.J. (2012). JNK signaling is the shared pathway linking neuroinflammation, blood-brain barrier disruption, and oligodendroglial apoptosis in the white matter injury of the immature brain. J. Neuroinflammation *9*, 175.

Xiao, Y., Jin, J., Chang, M., Nakaya, M., Hu, H., Zou, Q., Zhou, X., Brittain, G.C., Cheng, X., and Sun, S.C. (2014). TPL2 mediates autoimmune inflammation through activation of the TAK1 axis of IL-17 signaling. J. Exp. Med. *211*, 1689–1702.

Xu, D., Matsumoto, M.L., McKenzie, B.S., and Zarrin, A.A. (2018). TPL2 kinase action and control of inflammation. Pharmacol. Res. *129*, 188–193.

Zhong, Z., Deane, R., Ali, Z., Parisi, M., Shapovalov, Y., O'Banion, M.K., Stojanovic, K., Sagare, A., Boillee, S., Cleveland, D.W., and Zlokovic, B.V. (2008). ALS-causing SOD1 mutants generate vascular changes prior to motor neuron degeneration. Nat. Neurosci. *11*, 420–422.

STAR★METHODS

KEY RESOURCES TABLE

REAGENT or RESOURCE	SOURCE	IDENTIFIER
Antibodies		
Akt, rabbit polyclonal antibody	Santa Cruz	Cat# sc-8312; RRID:AB_671714
Albumin, sheep polyclonal antibody	Abcam	Cat# ab8940; RRID:AB_306875
B220, rat monoclonal antibody	BD Biosciences	Cat# 553084; RRID:AB_394614
B220, rat monoclonal antibody	BD Biosciences	Cat# 11-0112-85; RRID:AB_464936
B220, biotin-conjugated rat monoclonal antibody	eBioscience	Cat# 13-0452-82; RRID:AB_466449
CD105, rat monoclonal antibody	Biolegend	Cat# 120414; RRID:AB_2277914
CD11b, FITC-conjugated rat monoclonal antibody	eBioscience	Cat# 11-0112-41; RRID:AB_11042156
CD25, biotin-conjugated rat monoclonal antibody	BD Biosciences	553069; RRID:AB_394601
CD28, golden hamster monoclonal antibody	Biolegend	Cat# 102112; RRID:AB_312877
CD3, rabbit monoclonal antibody	Abcam	Cat# ab16669; RRID:AB_443425
CD3, PE-cy7-conjugated rat monoclonal antibody	eBioscience	Cat# 25-0031-82; RRID:AB_469572
CD3, biotin-conjugated rat monoclonal	eBioscience	Cat# 13-0452-82; RRID:AB_466449
CD3, Armenian hamster monoclonal antibody	Biolegend	Cat# 100314; RRID:AB_312679
CD31, rabbit polyclonal antibody	Abcam	Cat# ab28364; RRID:AB_726362
CD31, FITC-conjugated rat monoclonal antibody	BD Biosciences	Cat# 553372; RRID:AB_394818
CD31, rat monoclonal antibody	BD Pharmigen	Cat# 553369; RRID:AB_394815
CD34, rabbit monoclonal antibody	Abcam	Cat# ab81289; RRID:AB_1640331
CD4, Alexa700-conjugated rat monoclonal antibody	eBioscience	Cat# 56-0042-82; RRID:AB_494000
CD4, PE-conjugated rat monoclonal antibody	BD Biosciences	Cat# 553653; RRID:AB_394973
CD44, PE-conjugated rat monoclonal antibody	eBioscience	Cat# 12-0441-82; RRID:AB_465664
CD45, Alexa700-conjugated rat monoclonal antibody	Biolegend	Cat# 103128; RRID:AB_493715
CD8, FITC-conjugated rat monoclonal antibody	BD Biosciences	Cat# 553031; RRID:AB_394569
CD8, APC-conjugated rat monoclonal antibody	Biolegend	Cat# 100711; RRID:AB_312750
Claudin-5, mouse monoclonal antibody	Invitrogen	Cat# 35-2500; RRID:AB_2533200
Claudin-5, rabbit polyclonal antibody	Santa Cruz	Cat# sc-28670; RRID:AB_2260866
Claudin-5, rabbit polyclonal antibody	Invitrogen	Cat# 34-1600; RRID:AB_2533157
CTLA-4, PE-conjugated Armenian hamster monoclonal antibody	BD Biosciences	Cat# 553720; RRID:AB_395005
ERK, rabbit polyclonal antibody	Santa Cruz	Cat# sc-154-G; RRID:AB_631459
F4/80, rat monoclonal antibody	Serotec	Cat# MCA497GA; RRID:AB_323806
Fibrinogen, rabbit polyclonal antibody	Dako	Cat# F0111; RRID:AB_2335705
Foxp3, FITC-conjugated rat monoclonal antibody	eBioscience	Cat# 11-5773-82; RRID:AB_465243
GFAP, chicken polyclonal antibody	Abcam	Cat# ab4674; RRID:AB_304558
GL7, biotin-conjugated monoclonal antibody	eBioscience	Cat# 13-5902-85; RRID:AB_823153
ICAM-1, PE-conjugated Armenian hamster monoclonal antibody	BD Biosciences	Cat# 553253; RRID:AB_394735
ICAM-2, rat monoclonal antibody	BD Biosciences	Cat# 553326; RRID:AB_394784
IFN-γ, Alexa488-conjugated rat monoclonal antibody	Biolegend	Cat# 505813; RRID:AB_493312
IgD, APCcy7-conjugated rat monoclonal antibody	Biolegend	Cat# 405716; RRID:AB_10662544
IL-10, PE-conjugated rat monoclonal antibody	BD Biosciences	Cat# 554467; RRID:AB_395412
IL-17, Alexa647-conjugated rat monoclonal antibody	Biolegend	Cat# 506912; RRID:AB_536014
IκB, rabbit polyclonal antibody	Santa Cruz	Cat# sc-371; RRID:AB_2235952
JNK, mouse monoclonal antibody	Santa Cruz	Cat# sc-7345; RRID:AB_675864
Lamp2, mouse monoclonal antibody	Novus Biologicals	Cat# NBP2-22217; RRID:AB_2722697

(*Continued on next page*)

Continued

REAGENT or RESOURCE	SOURCE	IDENTIFIER
LFA-1, biotin-conjugated rat monoclonal	BD Biosciences	Cat# 557365; RRID:AB_2265094
NG2, mouse monoclonal antibody	R&D	Cat# MAB6689; RRID:AB_10890940
Occludin, goat polyclonal antibody	Santa Cruz	Cat# sc-8144; RRID:AB_653537
Occludin, rabbit polyclonal antibody	Invitrogen	Cat# 71-1500; RRID:AB_2533977
p38, mouse monoclonal antibody	Santa Cruz	Cat# sc-7972; RRID:AB_628079
p-Akt, rabbit polyclonal antibody	Santa Cruz	Cat# sc-101629; RRID:AB_2224735
p-ERK, mouse monoclonal antibody	Santa Cruz	Cat# sc-7383; RRID:AB_627545
p-IκB, mouse monoclonal antibody	Cell Signaling	Cat# 9246; RRID:AB_2267145
p-JNK, mouse monoclonal antibody	Cell Signaling	Cat# 9255; RRID:AB_2307321
p-p38, rabbit monoclonal antibody	Cell Signaling	Cat# 4631; RRID:AB_331765
Rab5, mouse monoclonal antibody	Abcam	Cat# ab66746; RRID:AB_1141650
Tpl2, rabbit polyclonal antibody	Santa Cruz	Cat# sc-720; RRID:AB_2140669
VCAM-1, Alexa647-conjugated rat monoclonal antibody	Biolegend	Cat# 105712; RRID:AB_493429
VE-cadherin, rat monoclonal antibody	eBioscience	Cat# 14-1441-81; RRID:AB_842768
VEGFR2, biotin-conjugated rat monoclonal antibody	Biolegend	Cat# 136409; RRID:AB_10564400
vWf, sheep polyclonal antibody	Abcam	Cat# ab11713; RRID:AB_298501
ZO-1, rabbit polyclonal antibody	Abcam	ab187012
β-actin, goat polyclonal antibody	Santa Cruz	Cat# sc-1615; RRID:AB_630835
β-tubulin, mouse monoclonal antibody	Santa Cruz	Cat# sc-58884; RRID:AB_793548
Biological samples		
See Table S1 for list of colon specimens from patients	Istituto Clinico Humanitas, this study	N/A
Chemicals, peptides, and recombinant proteins		
Collagenase I	Invitrogen	17018-029
Heparin	Sigma-Aldrich	H3149
Endothelial Cell Growth Supplement	Serotec	4110-5004
Human fibronectin	BD Biosciences	356008
Rat tail collagen I	BD Biosciences	354236
Dynabeads sheep anti-rat IgG	Invitrogen	11035
MG132	Sigma-Aldrich	M7449
Chloroquine	Tocris	4109
Marimastat	Tocris	2631
SP600125	Tocris	1496
Perifosine	Tocris	6087
SB203580	Tocris	1202
Collagenase/dispase	Roche	11097113001
TLCK (Nα-Tosyl-L-lysine chloromethyl ketone hydrochloride)	Sigma-Aldrich	90182
Percoll	Sigma-Aldrich	P1644-1L
ACCELL si Delivery Medium	Dharmacon	B-005000-100
Claudin-5 siRNA SMARTpool	Dharmacon	E-042358-00-0010
Accell Non-Targeting siRNA ()	Dharmacon	D-001910-01
Accell Mouse Control siRNA Kit – Green	Dharmacon	K-005000-G1-02
Recombinant mouse IL1β	Peprotec	211-11B
Recombinant human IL1β	Peprotec	200-01B
HiPerFect Transfection Reagent	QIAGEN	301707
DACC lipoplexes	Silence Therapeutics	Fehring et al., 2014

(*Continued on next page*)

Continued

REAGENT or RESOURCE	SOURCE	IDENTIFIER
MOG35-55 (MEVGWYRSPFSRVVHLYRNGK)	GeneCust	MOG35-55
Incomplete Freund's Adjuvant	Sigma-Aldrich	F5506
Mycobacterium tuberculosis H37Ra	Difco	DF3114-33-8
Pertussis toxin from Bordetella pertussis	Sigma-Aldrich	P2980
Tpl2 kinase Inhibitor	Calbiochem	616373
4 kDa FITC-Dextran	Sigma-Aldrich	46944
70 kDa FITC-Dextran	Sigma-Aldrich	46945
150 kDa FITC-Dextran	Sigma-Aldrich	74817
250 kDa FITC-Dextran	Sigma-Aldrich	FD250S
Zombie NIR Fixable Viability Kit	Biolegend	42315
Zombie Green Fixable Viability Kit	Biolegend	423111
Sytox Green Nucleic Acid Stain	Invitrogen	S7020
Propidium iodide	Sigma-Aldrich	255535-16-4
FITC Annexin V	BD Biosciences	556419
Recombinant mouse TNFα	Peprotech	315-01A
Recombinant mouse IL-2	Peprotech	212-12
Concanavalin A	Sigma-Aldrich	C5275
Ionomycin calcium salt from Streptomyces conglobatus	Sigma-Aldrich	I0634
RQ1 DNase	Promega	M6101
MMLV Reverse Transcriptase	Promega	28025013
Platinum SYBR-Green qPCR SuperMix	Invitrogen	11733046
Critical commercial assays		
In vitro Vascular Permeability assay	Millipore	ECM644
CellTrace CFSE Cell Proliferation Kit	Invitrogen	C34554
BD Cytofix/Cytoperm Plus Fixation/Permeabilization Kit	BD Biosciences	554715
Vectastain ABC kit	Vector Laboratories	PK-6100
ImmPACT® DAB Substrate, Peroxidase (HRP)	Vector Laboratories	SK-4105
Experimental models: Cell lines		
Human brain microvascular endothelial cells (HBMVEC)	Cell Systems	ACBRI 376
Experimental models: Organisms/strains		
Mice: $Tpl2^{F/F}$	Kollias Laboratory	Roulis et al., 2014
Mice: Tg(Tie1-cre)9Ref	Fassler Laboratory	Gustafsson et al., 2001
Mice: Tg(EIIa-cre)C5379Lmgd	Westphal Laboratory	Lakso et al., 1996
Mice: Tg(ITGAM-cre)2781Gkl	Cleveland Laboratory	Boillée et al., 2006
Mice: FVB-Tg(GFAP-cre)25Mes/J	The Jackson Laboratory	https://www.jax.org/strain/004600
Mice: B6.Cg-Tg(Nes-cre)1Kln/J	The Jackson Laboratory	https://www.jax.org/strain/003771
Mice: B6.129P2(Cg)-$Cx3cr1^{tm2.1(cre/ERT2)Litt}$/WganJ	The Jackson Laboratory	https://www.jax.org/strain/021160
Mice: Gt(ROSA)$26Sor^{tm4(ACTB-tdTomato,-EGFP)Luo}$/J	The Jackson Laboratory	https://www.jax.org/strain/007576
Oligonucleotides		
See Table S2 for oligonucleotide sequences	This study	N/A
Software and algorithms		
ImageJ	National Center for Microscopy and Imaging Research	RRID: SCR_003070

(*Continued on next page*)

Continued

REAGENT or RESOURCE	SOURCE	IDENTIFIER
GraphPad Prism	GraphPad	RRID: SCR_002798
Leica Application Suite X	Leica Microsystems	RRID: SCR_013673
FACSDiva	BD Biosciences	RRID: SCR_001456
FlowJo	Tree Star Inc	RRID: SCR_008520
Imaris	Oxford Instruments	RRID:SCR_007370

RESOURCE AVAILABILITY

Lead contact

Further information and requests for resources and reagents should be directed to and will be fulfilled by the lead contact, George Kollias (geokollias@med.uoa.gr).

Materials availability

Materials generated in this study are available from the corresponding author upon request.

Data and code availability

This study did not generate/analyze any datasets or code.

EXPERIMENTAL MODEL AND SUBJECT DETAILS

Human subjects

Intestinal tissues were obtained from surgical specimens taken from five patients suffering from Crohn's disease or ulcerative colitis. Sample information, including the age and gender of patients, is listed on Table S1. Healthy areas of intestine taken from patients admitted for bowel resection due to colon cancer or diverticulosis were used as controls. Human studies were approved by the Ethical Committee of Istituto Clinico Humanitas.

Mice

Conditional Tpl2 knockout mice were generated as previously described in Roulis et al.(2014). 3 *loxP* sites were introduced in the *Map3k8* locus, sequentially flanking a *neo* cassette and exon 4. Cre-mediated recombination produced the floxed ($Tpl2^{FF}$) mice. Tie1-Cre (Tg(Tie1-cre)9Ref), MGI:2385916) mice were provided by Reinhard Fassler (Max Planck Institute of Biochemistry). Ella-Cre (Tg(EIIa-cre)C5379Lmgd, MGI:2137691) mice were used for construction of the defloxed ($Tpl2^{DD}$) mice (Lakso et al., 1996). CD11b-Cre (Tg(ITGAM-cre)2781Gkl, MGI:3629092) were produced as described previously (Boillée et al., 2006). GFAP (FVB-Tg(GFAP-cre)25Mes/J, 00460), Nestin-Cre (B6.Cg-Tg(Nes-cre)1Kln/J, 003771), CX3CR1-CreERT2 (B6.129P2(Cg)-*Cx3cr1*$^{tm2.1(cre/ERT2)Litt}$/WganJ, 021160) and $ROSA^{mTmG}$ (*Gt(ROSA)26Sor*$^{tm4(ACTB-tdTomato,-EGFP)Luo}$/J, 007576) mice were purchased from Jackson Laboratory. In each experimental group, littermate controls and experimental mice caged together were used. CX3CR1-CreERT2 mice and controls were maintained in a tamoxifen diet for 4 weeks, then left untreated for 3 weeks before being submitted to EAE protocol. All mice used were maintained on a C57BL/6J genetic background and were housed in the conventional unit of the animal facilities in BSRC Alexander Fleming and used between 8 and 12 weeks of age. Only male mice were used for the EAE protocol, whereas for all other procedures both male and female mice were used (balanced in control and experimental groups).

Experiments were approved by the Institutional Committee of Protocol Evaluation in conjunction with the Veterinary Service Management of the Hellenic Republic Prefecture of Attika according to all current European and national legislation and were performed in accordance with relevant guidelines and regulations, under the relevant animal protocol licenses with number 3-07-2017/3801, 3-07-2017/3797, 26-11-2015/5758.

Primary lung endothelial cell culture

For *in vitro* assays, primary endothelial cells were isolated from lungs of 8-12 days old pups. Lungs were dissected, washed in HBSS containing antibiotics, passed briefly through 75% ethanol and then placed into DMEM with Penicillin/Streptomycin, FCS and glutamine. They were cut into 2- to 3-mm pieces and incubated with 0.1% collagenase I in PBS containing Ca^{2+} and Mg2+ for 30 minutes at 37°C. After homogenization using a 19G needle, the cell suspension was passed through a 70 μm cell strainer and centrifuged at 1500rpm for 5 minutes. The pellet was resuspended in medium containing equal volumes of DMEM low glucose (Invitrogen) and Ham's F-12 (Invitrogen), 20% FCS, Penicillin/Streptomycin (100 U/ml), Glutamine (2mM), Heparin (Sigma-Aldrich, 25mg/L) and endothelial mitogen (Serotec, 10 mL / 1 L medium). Cells were plated in T75 flasks pre-coated with 0.1% gelatine, 1% fibronectin and 1% collagen. For each culture, lungs from 6 pups were pulled together. ECs were further isolated with positive sorting, after

culturing of 2-3 days or when the cells were near confluency. Briefly, cells were incubated with antibody against ICAM-2 (BD Biosciences, 553326) for 1 hour at 4oC, and anti-rat IgG Dynabeads for 45 minutes at 4oC. After trypsinization and washes, the cell solution was placed in magnetic rack for isolation (Invitrogen). The cells that were retained on the beads were resuspended in EC medium and cultured in coated plates. They were used at passage 6 and checked for purity using FACs analysis with FACsCanto II (BD Biosciences). Cells were > 85% positive for VE-cadherin (eBioscience, 14-1441), CD31 (BD Biosciences, 553372), CD105 (Biolegend, 120414), VEGFR2 (Biolegend, 136409). In inhibitors treatment assays, adult mice were used for lung-derived endothelial cell isolation using the same protocol with minor modifications. After the incubation of the cells with the ICAM-2-coated magnetic beads, the cells were grown to confluency and a second positive selection was performed with CD31-coated magnetic beads (BD Pharmigen, 553369) in a similar fashion as prior step. Cells were treated with rmIL-1 purchased from Peprotec. All inhibitors used were commercially available and were used at optimized concentration; MG132 (0.2 μM; Sigma-Aldrich, M7449), chloroquine (20 μM; Tocris, 4109), marimastat (100 μM; Tocris, 2631), SP600125 (15 μM; Tocris, 1496), perifosine (10 μM; Tocris, 6087) and SB203580 (20 μM; Tocris, 1202).

Primary brain endothelial cell culture

Primary Brain Microvascular Endothelial Cells (BMVEC) were isolated from 8-12 weeks old mice, as previously described (Coisne et al., 2005) with minor adjustments. Brains were dissected and washed in isolation buffer (HBSS) containing antibiotics, 0.1% BSA and 10 mM HEPES. Brains were homogenized in isolation buffer in 7 mL Dounce homogenizer with 20 strokes of the loose pestle A and 20 strokes of the tight pestle B, and centrifuged at 240 g for 5 minutes at 4°C. Cell pellet was resuspended in pre-warmed digestion medium [DMEM low glucose (Invitrogen), 1mg/ml collagenase/dispase (Roche), 10 μg/ml DNAase I (Roche), 0.147 μg/ml TLCK], and incubated at 37°C for 30 minutes with gentle shaking. Tissue was centrifuged at 240 g for 5 minutes at 4°C, and the pellet was resuspended at 30% Percoll solution by vigorous shaking followed by centrifugation at 1000 g for 15 minutes at 4°C. The myelin-containing layer floating on top of the Percoll solution was poured off, and the cells were washed twice with HBSS. The pellet was resuspended in pre-warmed digestion medium and incubated at 37°C for 30 minutes with gentle shaking followed by two centrifugations at 240 g for 5 minutes at 4°C. The microvessel pellet was resuspended in BMVEC complete medium [equal volumes of DMEM low glucose and Ham's F-12, 20% FCS, Penicillin/Streptomycin (100 U/ml), Glutamine (2 mM), Heparin (Sigma-Aldrich, 100 mg/L) and endothelial mitogen (Serotec, 5 mg / 50 mL medium)]. Cells derived from 8 mice were plated in 10 wells of 24-well plate coated with 10 $\mu g/cm^2$ rat tail collagen I and 5 $\mu g/cm^2$ fibronectin in the presence of 3 μM puromycin, in order to eliminate all non-endothelial adherent cells by maintaining selective pressure on barrier-forming ECs. Culture medium was replaced after 3 days *in vitro* and then every 3rd day until the cells reached confluency. For claudin-5 siRNA transfection experiments cells were cultured for 72 hours in ACCELL siRNA Delivery Medium (Dharmacon B-005000-100) ± Claudin-5 siRNA SMARTpool (E-042358-00-0010) / Accell Non-Targeting siRNA (D-001910-01) / Accell Mouse Control siRNA Kit – Green (K-005000-G1-02) at 1 μM ± IL-1 10 ng/ml for the last 24 hours.

Primary astrocyte and microglia culture

Primary mixed glia cultures were isolated from brains of newborn mice (P4). After meninges removal, brains were cut into pieces and then digested in 0.25% trypsin at 37°C for 30 minutes. After incubation, the solution was passed through a 70 μm cell strainer followed by centrifugation at 1200 rpm for 10 minutes at room temperature. The pellet was resuspended in medium containing DMEM (Invitrogen), 20% FCS, Penicillin/Streptomycin (100 U/ml) and Glutamine (2 mM). Cells were plated in poly-D-lysine (PDL) coated plates. Medium was changed after 5 days *in vitro* and then every second day. When cells reached confluency, they were shaken for 3 hours at 37°C at 230 rpm to separate the astrocytes from microglia with astrocytes remaining attached to the culture plate. Cell purity was confirmed by FACS staining with antibodies against CD11b (eBioscience, 11-0112-41) and GFAP (Abcam, ab4674).

Cell lines

Human brain microvascular endothelial cells (HBMVEC, #ACBRI 376) were purchased from Cell Systems, cultured according to manufacturer's instructions and treated with hIL-1 and scrambled/Tpl2 siRNA (Invitrogen). *In vitro* transfections were performed with HiPerFect Transfection Reagent (QIAGEN) according to manufacturer's instructions for 72h.

METHOD DETAILS

B16Bl6 melanoma lung metastasis

B16Bl6 melanoma cells were cultured in complete RPMI medium and intravenously transferred to mice ($2x10^5$ cells per mouse). After 12 days, the mice were sacrificed and lungs were placed in Fakete's fixation solution. Metastatic nodules were enumerated in the stereoscope and lung sections were later processed for H&E staining and immunohistochemistry using antibodies against CD3 (Abcam, ab16669), B220 (BD Biosciences, 553084), F4/80 (Serotec, MCA497GA), CD34 (Abcam, ab81289), claudin-5 (Invitrogen, 35-2500) and VE-cadherin (eBioscience, 14-1441). The *in vivo* siRNA experiments were performed with DACC lipoplexes designed by Silence Therapeutics (Fehring et al., 2014). The siRNAs were manufactured by Biospring/Frankfurt and the sequences are reported at Table S2. The DACC siRNA formulations were administered intravenously (via tail vein) at a dose of 0.084mg/mouse at days 3, 5 and 7 post B16Bl6 intravenous delivery.

EAE induction

Male mice between 8 and 12 weeks of age were immunized subcutaneously into the side flanks with 100 μg MOG_{35-55} (MEVGWYRSPFSRVVHLYRNGK, GeneCust) in Incomplete Freund's Adjuvant (IFA) containing 1mg of heat-inactivated *Mycobacterium tuberculosis* H37Ra. Mice received two intraperitoneal injections of 100 ng pertussis toxin on day 0 and 2 after immunization. Animals were monitored daily for EAE symptoms and scored as follows: 0, no clinical disease; 1, tail weakness; 2, paraparesis (incomplete paralysis of 1 or 2 hind limbs); 3, paraplegia (complete paralysis of 1 or 2 hind limbs); 4, paraplegia with forelimb weakness or paralysis; 5, dead or moribund animal. EB and FITC-dextran intravenous injections in EAE mice were performed as described above.

In vivo permeability assays

Mice were injected with pyrilamine maleate salt (4 mg/kg in 0.9% saline; Sigma-Aldrich) 30 minutes before Evans blue (EB, Sigma-Aldrich) injection, in order to inhibit histamine release. EB (1% in sterile saline, 100 μl/mouse) was injected in the lateral vein of the tail and was left to circulate for 2 hours. rmIL-1 (100 ng/50 μl/mouse) was injected intradermally in the dorsal skin of the back or the ears. The adjacent side of the back or the other ear was injected with saline as control. 30 minutes after IL-1 injection, the skin was excised and EB was extracted by immersion in formamide at 55°C overnight. Basal extravasation was determined by excision of the kidney and lung. The amount of EB in the tissues was determined by spectrophotometric measurement at 620 nm. The amount of dye was determined from a standard curve and was normalized to the total tissue weight of each sample. For Tpl2 inhibitor experiments, Tpl2 kinase Inhibitor (Calbiochem, 616373) was administered intravenously for four consecutive days at 1.25 mg/kg before intradermal IL-1 administration. Control mice were injected with vehicle (saline/DMSO).

Mice were intravenously injected with different molecular weights FITC-dextran molecules (Sigma-Aldrich); 25 mg per mouse for the 4 kDa FITC-Dextran (in 100 μL volume of saline), 10 mg per mouse for the 70 kDa (in 200 μL volume of saline), 6.3 mg per mouse for the 150 kDa (in 200 μL volume of saline) and 5 mg per mouse for the 250 kDa (in 200 μL volume of saline). The 4 and 70 kDa FITC-dextran molecules were left to circulate for 10 minutes, whereas 150 kDa and 250 kDa FITC-dextran molecules were left for 4 hours. Tissues were dissected, embedded into cryoblocks, cut, and counterstained with DAPI fluoromount (Sigma-Aldrich).

In vitro permeability assay

The assay was performed according to manufacturer's instructions (Millipore, ECM644). Briefly, primary ECs were seeded onto the semi-permeable pre-coated with collagen insert and cultured to confluency. The cells were treated either with vesicle or rmIL-1 (10 ng/ml) for 24 hours. After 24 hours, the permeability treatment was removed and FITC-dextran was added to the semi-permeable insert coated with the EC for 60 minutes at room temperature. In the case of inhibitors, the cells were treated with IL-1 for 6 hours prior to inhibitors addition, and they were further incubated for 24 hours. 100 μL of medium was collected from the receiver tray, transferred to 96-well plate, and read in the fluorescent plate reader at 485 nm and 535 nm, excitation and emission, respectively.

Flow cytometry and antibodies

Mononuclear cell suspensions from draining inguinal lymph nodes and spinal cords were prepared according to standard protocols. Monocytes from spinal cords were isolated from the interphase of 35% / 70% isotonic Percoll gradient at room temperature. ECs from spinal cords were isolated after collagenase type I digestion from the interphase of HBSS / 45% isotonic Percoll gradient. Cell suspensions were stained for FACS analysis with the following antibodies against: CD4 (eBioscience, 56-0042-82), CD8 (BD Biosciences, 553031), CD11b (eBioscience, 11-0112-41), B220 (BD Biosciences, 11-0112-85), IL-10 (BD Biosciences, 554467), IFN-γ (Biolegend, 505813), IL-17 (Biolegend, 506912), CD31 (BD Biosciences, 553372), ICAM-1 (BD Biosciences, 553253), VCAM-1 (Biolegend, 105712), VE-cadherin (eBioscience, 14-1441), CD105 (Biolegend, 120414), VEGFR2 (Biolegend, 136409), Foxp3 (eBioscience, 11-5775-82), LFA-1 (BD Biosciences, 557365), CTLA-4 (BD Biosciences, 553720), CD45 (Biolegend, 103128), CD3 (eBioscience, 25-0031-82), CD4 (BD Biosciences, 553653), CD25 (BD Biosciences, 553069), CD44 (eBioscience, 12-0441-82), CD8 (eBioscience, 100711), GL7 (eBioscience, 13-5902-85), IgD (Biolegend, 405716). Live cells were gated as negative population Zombie NIR Fixable Viability Kit / Zombie Green Fixable Viability Kit (Biolegend, 42315/423111) / Sytox Green Nucleic Acid Stain (Invitrogen, S7020) / PI (Sigma-Aldrich, 255535-16-4). For biotin linked antibodies, APC / PE-TxR- / FITC / Alexa488 / Alexa647-streptavidin (BD Biosciences / Invitrogen) were used. Foxp3 staining was performed with Foxp3 Staining Buffer Set. For cell death assays, cells were stained with Annexin V and PI according to standard protocols in binding buffer. Cells were stimulated with plate-bound anti-CD3 (5 or 10 μg/ml; Biolegend, 100314), anti-CD3 and soluble anti-CD28 (Biolegend 102112) or TNF (1 μg/ml; Peprotech) for 24 hours *in vitro*. Cells were cultured for 48 hours with plate-bound anti-CD3 (5 μg/ml), stimulated for 48 hours with IL-2 (20 ng/ml; Peprotech) and then re-stimulated overnight with plate-bound anti-CD3 and IL-2. For proliferation assays, cells were stained with CFSE (Invitrogen) 5μM according to standard manufacturers' protocol and stimulated with Concanavalin A (4 μg/ml; Sigma-Aldrich) for 72 hours *in vitro*. Cells were stained with antibodies, run using the FACSCanto II (BD Biosciences) flow cytometer and analyzed with FlowJo (LLC) and DIVA (BD Biosciences) software tools.

In vitro cytokine production analysis

Intracellular cytokine staining was performed with BD Cytofix/Cytoperm (BD Biosciences) according to manufacturer's instructions. For intracellular cytokine staining, lymphocytes isolated from spinal cord and inguinal lymph nodes were cultured in 12-well plates in

complete RPMI for 24 hours and stimulated for 4 hours with PMA/ionomycin (Sigma-Aldrich) in the presence of Golgi Stop (BD Biosciences).

Western blot analysis

Cells or tissue samples were lysed in RIPA buffer containing 1% Triton X-100, 10mM Tris HCl (pH 7.4), 1 mM EDTA, 1% sodium deoxycholate, 0.1% SDS, 150 mM NaCl, protease inhibitors (Sigma-Aldrich) and phosphatase inhibitors (Sigma-Aldrich). Bradford assay (Bio-Rad) was used to determine total protein. Samples were subjected to SDS-PAGE and transferred to a nitrocellulose membrane (Whatman GmbH). Membranes were blocked and stained using antibodies raised against Tpl2 (1:500; Santa Cruz, sc-720), claudin-5 (1:1,000; Santa Cruz, sc-28670), claudin-5 (1:1,000; Invitrogen, 34-1600), occludin (1:5,000; Santa Cruz, sc-8144), occludin (1:,000; Invitrogen, 71-1500), p-ERK (1:1,000; Santa Cruz, sc-7383), p-JNK (1:1,000; Cell Signaling, 9255), p-p38 (1:1,000; Cell Signaling, 4631), p-Akt (1:1,000; Santa Cruz, sc-101629), p-IκB (1:1,000; Cell Signaling, 92465), β-actin (1:5,000; Santa Cruz, sc-1615), ERK (1:1,000; Santa Cruz, sc-154), JNK (1:1,000; Santa Cruz, sc-7345), p38 (1:1,000; Santa Cruz, sc-7972), IκB (1:1,000; Santa Cruz, sc-371), Akt (1:1,000; Santa Cruz, sc-8312) or β-tubulin (1:2,000; Santa Cruz, sc-58884) overnight at 4°C. For detection of phosphorylated proteins, the membranes were blocked with 5% BSA in TBS and all washes were performed with TBS (Tris-buffered saline) supplemented with 0.1% Tween-20. For all other proteins, 5% milk in PBS was used for washes and all washes were performed with PBS supplemented with 0.1% Tween-20. Secondary antibodies conjugated with HRP were purchased from Vector Laboratories and used at a concentration of 1:2,000 for 1 hour at room temperature. Signal development was performed with chemiluminescent HRP substrate (Immobilon Crescendo).

RNA extraction and RT-PCR

Spinal cords from mice (naive or 9 days post EAE induction) were harvested through hydraulic extrusion with HBSS. Each spinal cord was digested with 5ml of digestion medium (1.2 mg/ml collagenase/dispase mix, 0.1 mg/ml DNaseI, HBSS/10% FBS) for 55 minutes at 37°C with gentle shaking. Cells were centrifuged at 240 g for 5 minutes at 4°C, and the pellet was resuspended at 30% Percoll solution by vigorous shaking followed by centrifugation at 1000 g for 15 minutes at 4°C. The myelin-containing layer floating on top of the Percoll solution was poured off, and cells were washed twice with HBSS. Cells were incubated with ICAM-2-coated magnetic beads for 30 minutes at 4°C, and then with CD31-coated magnetic beads for another 30 minutes at 4°C. Endothelial cells were lysed in 400 μL TRI reagent (Sigma-Aldrich) per spinal cord and RNA extraction was performed according to manufacturer's instructions. After DNase treatment using RQ1 (Promega, M6101) and cDNA synthesis using M-MLV (Promega, 28025013). RT-PCR was performed using the primers found at Table S2 and the ΔΔCt method was used for quantification of relative mRNA levels.

Histology and immunofluorescence

For histological analysis, mice were perfused with PBS and tissues were dissected, fixed in formalin and embedded in paraffin. Paraffin-embedded tissues were deparaffinized (60°C for 30 minutes, de-wax in xylene, re-hydrate in descending grades of ethanol) and undergone antigen retrieval (acidic pH 6 or EDTA pH 8; according to antibody instructions) for 20 minutes in the microwave at full power. Spinal cord histology was performed with consecutive sections stained with Luxol Fast Blue (LFB) to assess demyelination and Luxol Fast Red (LFR) to assess inflammation, and other tissues were stained for H&E. Especially for Tpl2 immunohistochemistry, antigen retrieval was performed in 1mM EDTA (pH8)/0.1% Tween, at 65°C for 16 hours. Generally, sections were blocked with 1% BSA/PBS for 1 hour at room temperature, while endogenous peroxidase was blocked with 3% H_2O_2 for 10 minutes at room temperature. For immunofluorescence experiments, after PBS perfusion, tissues were dissected, fixed in 4% PFA and embedded in O.C.T. compound (VWR Chemicals), or snap-frozen in cryoblocks in O.C.T. compound in liquid nitrogen, or fixed in formalin and embedded in paraffin. For TJ visualization, fresh spinal cords were embedded in O.C.T. compound and fixation was performed in 100% ethanol at 4°C for 20 minutes and 100% acetone at −20°C for 6 minutes. For other spinal cord stainings, cryosections from fresh tissue were dried and fixed with ice-cold methanol. Antibodies used included GFAP (Abcam, ab4674), claudin-5 (Invitrogen, 35-2500), occludin (Invitrogen, 71-1500), albumin (Abcam, ab8940), fibrinogen (Dako, F0111), ZO-1 (Abcam, ab187012), ve-cadherin (eBioscience, 14-1441), CD3 (eBioscience, 13-0031-75), B220 (eBioscience, 13-0452-75), F4/80 (Serotec, MCA497GA), CD31 (Abcam, ab28364), CD31 (BD, 557355), NG2 (R&D, MAB6689), vWf (Abcam, ab11713), Lamp2 (Novus Biologicals, NBP2-22217) and Rab5 (Abcam, ab66746), and they were diluted in 1% BSA. For immunofluorescence, the secondary antibodies used were PE-Texas red anti-rat, FITC/Alexa Fluor 488/Alexa647–rabbit/rat/mouse IgG (Molecular Probes). For histology, biotin-conjugated anti-rabbit/rat/mouse IgG (Dako/Vector) were used as secondary antibodies with the Vectastain ABC kit (Vector Laboratories) to amplify the signal. Signal development was performed with DAB (3,3-diaminobenzidine) and hematoxylin was used as a counterstain. DAPI fluoromount (Sigma-Aldrich) was used for mounting fluorescence-stained sections and performing nuclear staining.

QUANTIFICATION AND STATISTICAL ANALYSIS

Image quantification

Quantification of histology experiments was performed by counting stained cells, as mentioned in main text. Quantification of immunofluorescence experiments was performed using ImageJ software after microscopy session performed in balanced samples (same number of experimental and control samples) with the same settings for all images. Integrated density values were recorded from

ImageJ (RawIntDen) for all samples and relative levels were calculated per microscopy session to combine multiple experiments. At least 20 images per mouse were quantified. For the *in vivo* permeability experiment quantification, Imaris software was used. In particular, single-plane confocal images were used (taken in a balanced manner from experimental and control samples with the same settings) and channels for green and red were created (FITC-dextran and CD31 staining, respectively). After background threshold adjustments, co-localization of the two channels was performed. Surfaces were created for all channels (green, red, and co-localization) and the Area values were recorded. The green Area value was reported after subtraction of the co-localized Area value. At least 15 images per mouse and condition were quantified. For lysosomal/endosomal staining experiments, Imaris software was used for quantification using the same analysis pipeline as with the *in vivo* permeability experiments with some differences. In particular, from the co-localized channel (CD31 and Lamp2, or CD31 and Rab5), the fluorescence intensity values were extracted and they were normalized to the area covered by CD31 signal to account for differential vascular coverage of the spinal cord sections.

Statistical analysis

Data in all experiments were analyzed with Prism software (GraphPad). Unpaired t test, one-way or two-way analysis of variance (ANOVA) tests were used for comparison of experimental groups depending on experimental procedure (figure legends specify tests used). P values of less than 0.05 were considered significant, and data were normally distributed with similar SEM between and within experimental groups. P values are depicted as * for $p < 0.05$, ** $p < 0.01$, *** $p < 0.001$ and **** $p < 0.0001$.